Quantitative comparison of vortex identification methods with applications

Author: Kinga Andrea Kovács

Supervisor: Dr. Esztella Balla

Faculty of Mechanical Engineering TDK - 2024

November 10, 2024

Contents

Abstract **3**

1 Introduction **5**

2 The applied vortex detection methods **7**
2.1 Classification of vortex identification methods 7
2.2 Requirements for vortex identification methods 7
2.3 Vortex identification methods under investigation 8
2.3.1 ω-criterion 8
2.3.2 Q-criterion 8
2.3.3 λ_2-criterion 9
2.3.4 Ω-method 10
2.3.5 Rortex/Liutex method 10
2.3.6 Omega-Liutex method 12
2.3.7 LAVD method 13

3 Simulation settings and results for the cylinder and the rectangular cuboid **14**
3.1 Geometrical model 14
3.2 Meshing of the flow field 14
3.3 Simulation settings and validation of the results 15

4 Quantitative comparison of the selected methods based on the cylinder and the rectangular cuboid simulations **17**
4.1 Comparison of the results on a selected test case (Re = 60, cylinder) 17
4.2 Testing the methods for the other simulation cases 21

5 Testing the methods on a circular arc cambered plate profile **25**
5.1 Introduction to cambered plates 25
5.2 The investigated case studies 25
5.3 Simulation settings 26

6 Mesh independence study **28**
6.1 Validation of the simulation results 29
6.2 Vortex detection 31

7 Testing the methods on PIV measurement data **34**

8 Conclusion and future outlook **39**

Acknowledgement **39**

References **44**

Appendix **45**

Abstract

The identification of vortices remains a critical yet unresolved challenge in the fluid mechanics community, as no universally accepted definition of a vortex exists. This study compares several vortex detection methods applied to the simulation of three-dimensional fluid flow around a cylinder and a rectangular cuboid at various Reynolds numbers and angles of attack. The methods evaluated include traditional Eulerian criteria – ω-criterion, Q-criterion, and λ_2-criterion – as well as more recent techniques such as the Ω-method, Rortex method, Omega-Liutex method, and the Lagrangian-averaged vorticity deviation (LAVD). Classification metrics and visualization techniques are used to quantify and compare the performance of each method. Additionally, the methods are tested on a case study involving two-dimensional simulations of flow around a circular arc cambered plate blade profile, commonly used in low-speed axial flow fans. These fans can experience noise and vibration due to the shedding of coherent vortex rows from the blades, making accurate vortex detection essential for potential geometric modifications. As an additional practical application the methods are also tested on Particle Image Velocimetry (PIV) measurement data concerning the generation of vortex rings produced by a vortex cannon. While traditional criteria like the ω-, Q-, and λ_2-criteria, as well as the Rortex method, can yield accurate results with carefully chosen parameters (for which no clear recommendations exist), newer approaches such as the Ω-method and Omega-Liutex method present practical solutions by addressing threshold-related issues, but they can still produce inaccurate results. The LAVD method, being threshold-independent, offers precise results but at the expense of significant computational time. For applications with limited computational resources, simpler methods like the Ω-method may be preferable. However, in scenarios requiring high accuracy, the LAVD method, despite its computational cost, is likely the most effective.

Author's note 1: From parts of the current study a journal paper entitled 'Quantitative comparison of vortex identification methods in three-dimensional fluid flow around cylinder geometries' with a manuscript number of HFF-D-24-01105 has been submitted to the International Journal of Heat and Fluid Flow. The paper is currently under revision.
Author's note 2: From parts of the current study a conference paper entitled 'Numerical investigation of the vortex shedding phenomenon from a circular-arc-cambered plate profile relevant to low-speed axial flow rotor blades', with a contribution ID of 185 has been submitted for the 16th European Turbomachinery Conference. The paper is currently under review.

Nomenclature

Abbreviations

CFD	Computational Fluid Dynamics
DeficiencyThresh	Convexity deficiency threshold [%]
LAVD	Lagrangian-averaged vorticity deviation
MinLength	Minimum arc-length threshold [%]
Nct	Number of contour levels to extract
PIV	Particle Image Velocimetry
PVS	Profile vortex shedding
RMS	Root-mean-square
SAS	Scale-Adaptive-Simulation
TE	Trailing edge

Greek letters

α	Local strain rate of fluid elements [s^{-1}]
β	Averaged angular velocity of fluid elements [s^{-1}]
$\boldsymbol{\omega}$	Vorticity [s^{-1}]
$\boldsymbol{\Omega}$	Angular rotation rate tensor or vorticity tensor [s^{-1}]
Δ	Absolute difference [%]
Δ_r	Relative error [%]
ϵ	Levi-Civita symbol
λ_1,λ_2,λ_3	Eigenvalues of $\boldsymbol{\Omega}^2 + \boldsymbol{S}^2$ [s^{-2}]
μ	Dynamic viscosity [$kg \cdot m^{-1} \cdot s^{-1}$]
$\overline{\boldsymbol{\omega}}$	Spatial mean of vorticity [s^{-1}]
θ	Angle of incidence [°]
ε	Small positive number to eliminate noise or avoid division by zero [s^{-2}]
Ω	Values for the Ω-method
Ω_R	Values for the Omega-Liutex method
ϱ	Density [$kg \cdot m^{-3}$]
ϑ	Angle of rotation [°]

Roman letters

$\boldsymbol{a}$	Constant velocity vector [$m \cdot s^{-1}$]
$\boldsymbol{b}(t)$	Time-dependent translation vector [m]
$\boldsymbol{G}$	Velocity gradient tensor [s^{-1}]
$\boldsymbol{N}$	Non-rotational part of the vorticity tensor [s^{-1}]
$\boldsymbol{P}$	Rotation matrix around the Z-axis
$\boldsymbol{Q}$	Proper orthogonal tensor
$\boldsymbol{Q}$(t)	Time-dependent proper orthogonal tensor
$\boldsymbol{Q}_r$	Orthogonal rotation matrix from the xyz-frame to the XYZ-frame
$\boldsymbol{R}$	Rotational part of the vorticity tensor, Rortex (vortex vector) [s^{-1}]
$\boldsymbol{r}$	Unit vector in the direction of rotation in the xyz-frame
$\boldsymbol{S}$	Strain rate tensor or deformation tensor [s^{-1}]
$\boldsymbol{v}$	Velocity [$m \cdot s^{-1}$]
$\boldsymbol{x}(t, \boldsymbol{x}_0)$	Instantaneous particle positions [m]
$\boldsymbol{x}_0$	Initial particle positions [m]
Re	Reynolds number
Re_c	Chord-based Reynolds number
St	Strouhal number
St^*	Universal Strouhal number
$\nabla \boldsymbol{V}$	Velocity gradient tensor in the XYZ-frame [$m \cdot s^{-1}$]
$\nabla \boldsymbol{v}$	Velocity gradient tensor in the xyz-frame [$m \cdot s^{-1}$]
A	Accuracy
a	Square of the Frobenius norm of the strain rate tensor [s^{-2}]
b	Square of the Frobenius norm of the vorticity tensor [s^{-2}]
$B(t)$	Boundary of a rotationally coherent Lagrangian vortex
b_t	Transversal distance between the shed vortex rows [m]
c	Chord length [m]
$C(t)$	Center of a rotationally coherent Lagrangian vortex
c_D	Drag coefficient
c_L	Lift coefficient
D	Cylinder diameter [m]
d	Characteristic length [m]
$D(t)$	Rotationally coherent Lagrangian vortex
f	Vortex shedding frequency [Hz]
g_Z	The criterion of rotation of fluid element in 2D [s^{-2}]
h	Side length of the square [m]
N	Number of cells
P	Precision
p	Order of convergence
Q	Second invariant of the velocity gradient tensor [s^{-2}]
R	Recall
R_Z	Magnitude of Rortex [s^{-1}]
t	Final time instant of the integration [s]
t_0	Starting time instant of the integration [s]
U_0	Inlet velocity [$m \cdot s^{-1}$]
y^+	Dimensionless wall distance
$F1$	F1 score
FN	False negative
FP	False positive
TN	True negative
TP	True positive
Ma	Mach number

1 Introduction

What is a vortex? This seemingly simple, but fundamental question still has no universally accepted answer. The proper identification of vortices is of great interest within the fluid mechanics community. However, since there does not exist an exact vortex definition, the number of vortex detection methods is relatively high. Each method has its advantages and disadvantages, but currently there is no consensus among researchers regarding which method is the best and the most widely applicable.

Vortex as a phenomenon itself, is common both in nature (e.g., von Karman vortex streets in the wake of islands [1], Borneo vortex [2]), and in our everyday lives (e.g., bathtub vortex [3]). Vortices also play important roles in our health (e.g., vortices in blood flow [4]). Moreover, the accurate detection of vortices is vital in several practical engineering applications, e.g., drip irrigation [5]. In the case of hydroturbines, vortices are typical flow structures and they can lead to various kinds of instabilities (e.g., pressure fluctuations, noise generation, vibrations, cavitation erosion and material fatigue). In some extreme cases they can even affect the safety of the operation, therefore, it is vital to detect and analyze vortical structures in such applications [6]. Apart from hydroturbines, vortices also play very important roles in the aerodynamics of airfoils [7], wind turbine dynamics [8], low-speed axial fan operations [9], and vortex mixers [10]. The listed application fields are only a smidgen of the actual number of possible applications. Therefore, it can be seen that methods for the identification of vortices are crucial in fluid dynamics for analyzing the underlying vortical structures and to better understand vortex formation.

The aim of the current study is to compare various vortex detection methods in the case of three-dimensional Computational Fluid Dynamics (CFD) simulation of fluid flow around a cylinder and a rectangular cuboid at multiple Reynolds numbers and angles of attack. There are similar studies in the literature concerning the comparison of vortex identification methods [6, 11, 12, 13, 14]. In these papers the comparison of the detection methods is qualitative. In the current study, however, classification metrics commonly used in machine learning are applied to enable a quantitative comparison of the detection methods. In addition to bluff bodies, the selected methods are also tested on a case study involving two-dimensional compressible CFD simulations of flow around a circular arc cambered plate profile, representing streamlined bodies. Circular arc cambered plate profiles are often applied in low-speed axial flow fans [15, 16] due to their relatively low manufacturing cost and simple manufacturing technique. Additionally, the methods are tested on Particle Image Velocimetry (PIV) measurement data concerning the generation of vortex rings produced by a vortex cannon to examine their performance in experimental scenarios.

The methods under investigation include basic Eulerian local (region-type) vortex identification methods, these are the following: ω-criterion, Q-criterion [17], and λ_2-criterion [18]. These criteria are relatively easy to implement, and fast to compute, however, they suffer from some common issues [19]:

1. They are based on arbitrarily chosen threshold values.
2. The physical meaning of these threshold values is unclear.
3. Inappropriate thresholds can lead to capturing strong vortices, but skipping weak ones.

Apart from these widespread methods, four relatively new vortex identification methods are also examined. Recently Liu et al. proposed the Ω-method [19] with which the aim was to overcome the aforementioned weaknesses. Supposedly, by setting the threshold value to 0.52,

satisfactory detection results can be obtained, thus eliminating the necessity of an arbitrarily chosen threshold value. It is important to mention though, that this value is empirical, and it is not derived from any physical principle, therefore it is just as arbitrary as the other threshold values. Another vortex identification method to be examined is the Rortex method (or Liutex method) proposed by Tian et al. [20]. They proposed a definition of a new vector quantity which is called the vortex vector (Rortex). This new vector can provide both the swirling strength, and the local rotational axis. In addition, the Rortex method can distinguish the rotational vortices from the shear layers (in which high vorticity values are present). In order to merge the advantages of the Ω-, and Rortex methods, the so-called Omega-Liutex method was proposed by Dong et al. [21]. This method can distinguish vortical motion from vorticity caused by shear flow, and they state that it does not depend on an arbitrarily chosen threshold value. Similarly to the Ω-method the threshold value here is also empirical, therefore it cannot be stated that the need for a threshold value is eliminated. Lastly, another promising vortex detection criterion was proposed by Haller et al. [22] called the Lagrangian-averaged vorticity deviation (LAVD). Haller et al. [22] define vortices as a nested set of material tubes which exhibit uniform instrinsic material rotation. This criterion is based on the trajectory integral of the absolute difference between the vorticity and its spatial mean. One of the advantages of the LAVD method is that it does not require an arbitrarily chosen threshold value. The author agrees with the latter definition, meaning, a vortex is a region of the flow in which material elements experience the same rotation.

In order to quantify the accuracy of the selected methods, different classification metrics are determined, and the visualization of the detection results is also provided. The following steps outline the process:

1. Based on the simulation results the ω, Q, λ_2, Ω, Rortex, Omega-Liutex, and LAVD fields are calculated.

2. Various threshold values are applied for the ω, Q, λ_2, Ω, Rortex, and Omega-Liutex fields to identify vortices, and the vortex detection is performed with the LAVD method as well.

3. Classification metrics are determined, and they are plotted against the applied threshold values to examine how sensitive the detection results are to the different isovalues.

4. The visualization of the detection results is performed.

The general outline of the current study is as follows. In the next section, vortex identification methods are introduced in general, with a detailed description of the above-mentioned selected methods. In the third section, the simulation settings for the cylinder and the rectangular cuboid geometries are briefly described. Afterwards, in the fourth section, comparison between the different methods is performed through vortex detection in the wake of the cylinder, and the rectangular cuboid geometries. The results are analyzed, and the differences between the selected methods and their advantages and disadvantages are detailed. In section five the simulation settings and results with respect to the cambered plate geometry are introduced. In addition, the detection results obtained with the different detection methods are also presented. In section six, the methods are evaluated using PIV measurement data in connection with vortex ring collision. Lastly, in section seven, concluding remarks of the present study are given among with suggestions for future research plans.

2 The applied vortex detection methods

2.1 Classification of vortex identification methods

In general, vortex identification methods can be classified as *Eulerian* and *Lagrangian* methods [23]. Eulerian methods are derived from *Eulerian quantities* (such as velocity gradients), and Lagrangian methods are derived from *Lagrangian quantities* (such as particle pathlines). Eulerian methods can be further divided into *local* and *non-local* methods. Local methods are evaluated pointwise, and non-local methods depend on multiple points in the domain. Eulerian local methods can be further classified as *region-type* and *line-type methods*. Eulerian local region-type methods are the most widespread vortex identification methods, because they depend only on the instantaneous velocity field and can be computed pointwise. Region-type methods (e.g., ω-criterion, Q-criterion, λ_2-criterion) depend on arbitrarily chosen threshold values, and they define the vortex core within a region in which a given scalar function falls below (or above) the predefined threshold value. On the other hand, line-type methods extract the vortex core lines, e.g., vorticity-predictor and pressure corrector scheme [24].

2.2 Requirements for vortex identification methods

Several requirements have been formulated by different authors in connection with vortex identification methods. An ideal vortex identification criterion should fulfill the following requirements [23, 25]:

- objectivity (i.e., frame indifference; however, many authors only require Galilean invariance),
- validity for compressible flows,
- avoidance of the usage of arbitrarily chosen threshold values,
- applicability for imperfect velocity data (e.g., measurement data),
- ensurance of nonzero vorticity within the vortex to exclude regions of irrotational flow,
- guarantee of coherent motion of material particles within the vortex (i.e., particle separation remains small),
- discrimination against vorticity due to shear flow,
- identify the swirl axis and orientation,
- determination of the integral vortex strength.

The concept of objectivity [26] is important in mechanics, and it requires that the response of a material is independent of the observer. In the present context this means that the same region should be identified as a vortex (by a given criterion) regardless of arbitrary translation or rotation of the observer [23]. Mathematically this means that the detection criterion should be invariant under coordinate changes of the form:

$$\boldsymbol{x}^* = \boldsymbol{Q}(t)\boldsymbol{x} + \boldsymbol{b}(t), \tag{2.1}$$

where $\boldsymbol{Q}(t)$ is a time-dependent proper orthogonal tensor, and $\boldsymbol{b}(t)$ is a time-dependent translation vector.

As for Galilean invariance, this encloses criteria that remain invariant under coordinate changes of the form [27]:

$$\boldsymbol{y} = \boldsymbol{Q}\boldsymbol{x} + \boldsymbol{a}t, \tag{2.2}$$

where $\boldsymbol{Q}$ is a proper orthogonal tensor, and $\boldsymbol{a}$ is a constant velocity vector. Galilean invariance is the special case of static rotation, and a constant velocity translation [23].

At this point the following question arises: *is Galilean invariance sufficient or is objectivity needed?* Jeong et al. only require Galilean invariance from detection methods [18]. On the other hand, the need for objectivity has been pointed out by several authors [28, 29, 30]. Haller [28] argues and states that Galilean-invariant criteria give consistent results in frames that move at constant speeds relative to each other. The same criteria, however, fail to be invariant under more general changes of frame such as rotations [28]. The author here agrees that objectivity is needed.

2.3 Vortex identification methods under investigation

Seven different vortex identification methods were chosen for the comparison, these are the following: ω-criterion, Q-criterion, λ_2-criterion, Ω-method, Rortex method, Omega-Liutex method, and the LAVD method. The selected methods are detailed below.

2.3.1 ω-criterion

The ω-criterion is an Eulerian local (region-type) vortex identification criterion, which states that there exists a vortex in a simply connected region if:

$$|\boldsymbol{\omega}| > \omega_{\text{thresh}}, \tag{2.3}$$

where $\boldsymbol{\omega}$ denotes the vorticity, which is defined as the curl of the velocity: $\boldsymbol{\omega} \equiv \boldsymbol{\nabla} \times \boldsymbol{v}$, and ω_{thresh} denotes the arbitrarily chosen threshold value. Upon initial observation, this method appears to be the most straightforward when trying to detect vortices, however, it has been emphasized by many authors that it is not suitable for the detection of vortices, because it cannot differentiate between pure shearing motions, and the actual swirling motion of a vortex [25]. Shear layers have large vorticity values, however, they do not induce whirling motion [23]. For instance, in the case of a laminar boundary layer, high vorticity is present, though there is no rotational motion. Moreover, this criterion is not objective, and it depends on an arbitrarily chosen threshold.

2.3.2 Q-criterion

Probably one of the most widespread, and well-known vortex identification methods is the Q-criterion, which is Galilean invariant, and it is based on the velocity-gradient tensor, denoted by $\boldsymbol{G}$ herein. It is defined as $\boldsymbol{G} = \nabla \boldsymbol{v}$, and it can be decomposed into symmetric and anti-symmetric parts:

$$\boldsymbol{G} = \boldsymbol{S} + \boldsymbol{\Omega}, \tag{2.4}$$

where $\boldsymbol{S} = \frac{1}{2}[\boldsymbol{G} + \boldsymbol{G}^{\mathrm{T}}]$ is the strain rate tensor, and $\boldsymbol{\Omega} = \frac{1}{2}[\boldsymbol{G} - \boldsymbol{G}^{\mathrm{T}}]$ is the angular rotation rate tensor. The connection between the vorticity vector (introduced in *Section 2.3.1*) and the angular rotation rate tensor can be expressed in the following way:

$$\boldsymbol{\Omega}_{ij} = \frac{1}{2}\epsilon_{ijk} \cdot \omega_k, \tag{2.5}$$

where ϵ is the Levi-Civita symbol or permutation symbol, defined in the following way:

$$\epsilon_{ijk} = \begin{cases} 1 & \text{for even permutation of } ijk, \\ -1 & \text{for odd permutation of } ijk, \\ 0 & \text{if there is a repeated index.} \end{cases} \tag{2.6}$$

The velocity gradient tensor describes the average deformation and rotation of a fluid element [23]. Hunt et al. defined vortices in the following way (Q is the second invariant of $\boldsymbol{G}$) [17]:

1. $Q = \frac{1}{2}(\|\boldsymbol{\Omega}\|^2 - \|\boldsymbol{S}\|^2) > 0.$

where $\|\cdot\|$ is the Frobenius norm. It is important to mention that during vortex detection the following criterion is used: $Q > Q_{\text{thresh}}$, where Q_{thresh} is an individually chosen threshold value, which is not necessarily equal to zero and has to be fine-tuned.

Based on the Q-criterion, a vortex exists where there is more rotation than stretching [23]. The problem with this method is that it depends on an arbitrarily chosen threshold value, and the physical meaning of the Q values cannot be interpreted. Setting the threshold too low can lead to the detection of physically meaningless vortices, whereas setting the threshold too high can result in the elimination of physically meaningful vortices.

2.3.3 λ_2-criterion

The λ_2-criterion was proposed by Jeong et al. [18], and similarly to the Q-criterion it is also Galilean invariant. It was formulated based on the notion that a pressure minimum should exist across a vortex core, however, the pressure minimum in itself cannot be used as a general identification criterion for vortices. This is due to two main effects:

- Unsteady straining, which can create a pressure minimum without involving a vortical or swirling motion.
- Viscous effects, which can eliminate the pressure minimum in a flow with vortical motion.

In order to ignore these unsteady and viscous effects while looking for pressure minimum they formulated the λ_2-criterion. They define a vortex core as a connected region with two negative eigenvalues of $\boldsymbol{\Omega}^2 + \boldsymbol{S}^2$. Since $\boldsymbol{\Omega}^2 + \boldsymbol{S}^2$ is symmetric, it has real eigenvalues only, and if the eigenvalues are ordered in the following manner: $\lambda_1 \geq \lambda_2 \geq \lambda_3$, then this definition is equivalent with the following criterion:

$$\lambda_2 < 0. \tag{2.7}$$

Similarly to the Q-criterion, during the detection the threshold value typically differs from zero in order to eliminate artificial vortices and fine-tune the vortex detection results. It is important to mention that for incompressible flows $Q = -\frac{1}{2}(\lambda_1 + \lambda_2 + \lambda_3)$ [18]. Therefore, the Q and λ_2 criteria are not redundant, i.e., these two definitions do not necessarily agree. While the Q-criterion measures the excess of rotation rate over the strain rate magnitude in all directions, the λ_2-criterion looks for this excess only on a specific plane [31]. Similarly to the Q-criterion, the same problem arises. Meaning, the chosen threshold value is a matter of individual (subjective) judgement, and setting it too low/high can lead to incorrect detection results. In addition, the physical meaning of the λ_2 values is unclear.

2.3.4 Ω-method

The Galilean invariant Ω-method was introduced by Liu et al. [19], and the main idea is that vorticity should be split into a vortical part and a non-vortical part, because vorticity does not directly represent rotation. The author here would like to make a comment: the $\boldsymbol{\Omega}$ tensor is called the angular rotation rate tensor in the majority of the literature, however, Liu et al. [19, 32] call it as the vorticity tensor, because they state that the anti-symmetric part of the velocity gradient tensor is related to vorticity rather than the global rotation. They then state that vorticity should be further decomposed into two parts: one is vortical vorticity contributed to rotation and the other one is non-vortical vorticity [19]. Vorticity can be small while rotation is strong, and vorticity can be large when rotation is weak or basically none. Ω is then defined as the ratio of the vorticity tensor norm squared over the sum of the vorticity tensor norm squared and the deformation tensor (or strain rate tensor) norm squared [32].

$$\Omega = \frac{\|\boldsymbol{\Omega}\|^2}{\|\boldsymbol{S}\|^2 + \|\boldsymbol{\Omega}\|^2 + \varepsilon} = \frac{b}{a + b + \varepsilon}, \tag{2.8}$$

where $a = \|\boldsymbol{S}\|^2$, $b = \|\boldsymbol{\Omega}\|^2$, and ε is a small positive number used to avoid division by zero [19], and to reduce or even remove some serious noises that can appear in the flow domain if both a and b are close to zero [32]. The properly adjusted value of ε is case-related, and dimension-related. According to Dong et al., based on a large number of test results from different cases an expression for the value of ε is proposed [33]:

$$\varepsilon = 0.001 \cdot (b - a)_{\max} = 0.002 \cdot Q_{\max}, \tag{2.9}$$

where $Q_{\max}$ is the maximum of the Q values for a given time step, because one may recall that $Q = \frac{1}{2}(b - a)$.

The Ω-method requires a limit larger than 0.5, and in practice $\Omega = 0.51$ or $\Omega = 0.52$ can be used as the fixed threshold [32]. At $\Omega = 1$ the fluid becomes a rigid body, and this indicates no deformation. Liu et al. also state that the Ω-method is insensitive to moderate threshold changes, however, its sensitivity is not quantified [32] (this is performed in the current study). It must also be mentioned that the selection of $\Omega = 0.52$ is only empirical for the approximation of vortex boundaries, and it is not derived from any physical principle.

2.3.5 Rortex/Liutex method

The Rortex method was proposed by Tian et al. [20]. They state that though Liu et al. [19] pointed out that vorticity should be decomposed into a rotational ($\boldsymbol{R}$) and a non-rotational ($\boldsymbol{N}$) part, they did not show how to decompose the vorticity and did not give formulae for $\boldsymbol{R}$, and $\boldsymbol{N}$. Tian et al. [20] presented the mathematical definition of the rotational part of the vorticity, vortex vector $\boldsymbol{R}$ to describe the fluid rotation. The rotational part is called the Liutex/Rortex vector, which can represent both the direction and magnitude of the rotational motion.

The direction of Rortex is determined by the direction of the local rotation axis Z, and the magnitude is defined by the rotational strength of the local fluid rotation, which is determined in the XY plane perpendicular to the Z-axis [34]. At first, the original xyz-frame is transformed to a new XYZ-frame. The velocity gradient tensors in the different frames are the following [35]:

$$\nabla \boldsymbol{v} = \begin{bmatrix} \frac{\partial u}{\partial x} & \frac{\partial u}{\partial y} & \frac{\partial u}{\partial z} \\ \frac{\partial v}{\partial x} & \frac{\partial v}{\partial y} & \frac{\partial v}{\partial z} \\ \frac{\partial w}{\partial x} & \frac{\partial w}{\partial y} & \frac{\partial w}{\partial z} \end{bmatrix}, \quad \nabla \boldsymbol{V} = \begin{bmatrix} \frac{\partial U}{\partial X} & \frac{\partial U}{\partial Y} & \frac{\partial U}{\partial Z} \\ \frac{\partial V}{\partial X} & \frac{\partial V}{\partial Y} & \frac{\partial V}{\partial Z} \\ \frac{\partial W}{\partial X} & \frac{\partial W}{\partial Y} & \frac{\partial W}{\partial Z} \end{bmatrix}. \tag{2.10}$$

The relation between the coordinate systems is the following:

$$\nabla \boldsymbol{V} = \boldsymbol{Q}_r \nabla \boldsymbol{v} \boldsymbol{Q}_r^{-1}, \tag{2.11}$$

where $\boldsymbol{Q}_r$ is an orthogonal rotation matrix from the xyz-frame to the XYZ-frame. To prove the existence, and to obtain the direction of the local rotation axis Z, real Schur decomposition, and the Newton iterative method was applied by Tian et al. [20].

In order not to have rotation around the X- and Y-axes the following criteria has to be fulfilled:

$$\frac{\partial U}{\partial Z} = 0, \tag{2.12}$$

$$\frac{\partial V}{\partial Z} = 0. \tag{2.13}$$

Therefore the velocity gradient tensor in the XYZ-frame is going to have the following form:

$$\nabla \boldsymbol{V} = \begin{bmatrix} \frac{\partial U}{\partial X} & \frac{\partial U}{\partial Y} & 0 \\ \frac{\partial V}{\partial X} & \frac{\partial V}{\partial Y} & 0 \\ \frac{\partial W}{\partial X} & \frac{\partial W}{\partial Y} & \frac{\partial W}{\partial Z} \end{bmatrix}. \tag{2.14}$$

If the direction of the Z-axis in the xyz-frame is given by $\boldsymbol{r} = [r_x, r_y, r_z]^{\mathrm{T}}$, then [34]:

$$\boldsymbol{r} = \boldsymbol{Q}_r^T \begin{bmatrix} 0 \\ 0 \\ 1 \end{bmatrix}, \tag{2.15}$$

and:

$$\boldsymbol{Q}_r \boldsymbol{r} = \begin{bmatrix} 0 \\ 0 \\ 1 \end{bmatrix} \tag{2.16}$$

represents the direction of the local rotation axis Z in the XYZ-frame.

At this point the rotation strength, which represents the local rigid rotation, is still needed [35]. This can be obtained with the help of a second coordinate rotation in plane XY. The XYZ-frame is rotated around the Z-axis with an angle ϑ. The new velocity gradient tensor is going to be the following:

$$\nabla \boldsymbol{V}_\vartheta = \boldsymbol{P} \nabla \boldsymbol{V} \boldsymbol{P}^{-1}, \tag{2.17}$$

where $\boldsymbol{P}$ is the rotation matrix around the Z-axis:

$$\boldsymbol{P} = \begin{bmatrix} \cos\vartheta & \sin\vartheta & 0 \\ -\sin\vartheta & \cos\vartheta & 0 \\ 0 & 0 & 1 \end{bmatrix}. \tag{2.18}$$

Based on this, the elements of the 2×2 upper left submatrix of the transformed velocity gradient tensor can be obtained [20, 32, 34, 35]. In addition, the following parameters can be introduced [35]:

$$\alpha = \frac{1}{2} \sqrt{\left(\frac{\partial V}{\partial Y} - \frac{\partial U}{\partial X} \right)^2 + \left(\frac{\partial V}{\partial X} + \frac{\partial U}{\partial X} \right)^2}, \tag{2.19}$$

$$\beta = \frac{1}{2} \left(\frac{\partial V}{\partial X} - \frac{\partial U}{\partial Y} \right), \tag{2.20}$$

where α is the local strain rate of fluid elements, and β is the averaged angular velocity of fluid elements.

The criterion to determine the existence of local fluid rotation in the XY plane is as follows [34]:

$$g_{Z\min} = \beta^2 - \alpha^2 > 0, \tag{2.21}$$

and the local rotation strength (the magnitude of Rortex) is defined in the following way (it is assumed that $\beta > 0$):

$$R_Z = \begin{cases} 2(\beta - \alpha), & g_{Z\min} > 0, \\ 0, & g_{Z\min} \leq 0. \end{cases} \tag{2.22}$$

The vortex vector representing the local fluid rotation is defined in the following way:

$$\boldsymbol{R} = R_Z \boldsymbol{r}, \tag{2.23}$$

where $\boldsymbol{r}$ is the unit vector in the direction of the rotation axis in the xyz-frame, and there exists a vortex if $R_Z \neq 0$ [35]. By relying on the above-described definition, the usage of Newton iteration or real Schur decomposition is needed which makes the implementation more difficult. In order to avoid the usage of said things, Gao et al. [34] proposed an eigenvector-based definition, and in the current paper the detection was implemented based on the latter.

The direction of the local rotation axis ($\boldsymbol{r}$) is the real eigenvector of the velocity gradient tensor $\nabla \boldsymbol{v}$, and according to Eq. (2.16), $\boldsymbol{Q}_r \boldsymbol{r}$ is the direction of local rotation in the XYZ-frame, where $\boldsymbol{Q}_r$ is the rotation tensor which rotates the z-axis to the direction of $\boldsymbol{r}$. The vector $\begin{bmatrix} 0 & 0 & 1 \end{bmatrix}^{\mathrm{T}}$ is the real eigenvector of $\nabla \boldsymbol{V}$ in the XYZ-frame, and $\boldsymbol{r} = \boldsymbol{Q}_r^{\mathrm{T}} \begin{bmatrix} 0 & 0 & 1 \end{bmatrix}^{\mathrm{T}}$ represents the real eigenvector of the velocity gradient tensor $\nabla \boldsymbol{v}$ in the xyz-frame. The definition of the rotational strength is the same as before.

2.3.6 Omega-Liutex method

The Ω-method has the advantage that it does not need an arbitrarily chosen threshold value (though it is important to emphasize again that the value of $\Omega = 0.52$ is empirical, and it is not derived from any physical principle), and the Rortex method has the advantage that it can differentiate between rotational vortices and shear layers. In order to merge the benefits of these methods a new vortex identification method was proposed by Dong et al. [21] called the Omega-Liutex method. The basic idea is that the α and β values are determined just like in the case of the Rortex method, and afterwards Ω_R (representing the Omega-Liutex field) is defined in the following practical manner:

$$\Omega_R = \frac{\beta^2}{\alpha^2 + \beta^2 + \varepsilon}, \tag{2.24}$$

where ε (similarly to the Ω-method) is a small parameter introduced in the denominator of Ω_R to remove the noises caused by rounding errors. ε can be defined in the following way:

$$\varepsilon = 0.001 \cdot (\beta^2 - \alpha^2)_{\max}, \tag{2.25}$$

where the value of $(\beta^2 - \alpha^2)_{\max}$ is fixed for each time step, and can be determined easily. Afterwards, similarly to the Ω-method $\Omega_R = 0.52$ can be chosen to visualize the vortex structures.

2.3.7 LAVD method

The Lagrangian-averaged vorticity deviation (LAVD) method was proposed by Haller et al. [22]. They define a rotationally coherent Lagrangian vortex as a nested set of material tubes, each exhibiting uniform intrinsic material rotation. Such a vortex turns out to be foliated by outward-decreasing tubular level sets of the Lagrangian-averaged vorticity deviation [22]. The LAVD is derived from the dynamic rotation tensor, which is obtained from the dynamic polar decomposition of the deformation gradient. This provides an objective global vortex criterion which is entirely frame-invariant, and mathematically it can be expressed in the following manner (it is the trajectory integral of the absolute difference between the vorticity and its spatial mean):

$$\mathrm{LAVD}_{t_0}^{t}(\boldsymbol{x}_0) := \int_{t_0}^{t} \left| \boldsymbol{\omega}\big(\boldsymbol{x}(s;\boldsymbol{x}_0), s\big) - \overline{\boldsymbol{\omega}}(s) \right| \mathrm{d}s, \tag{2.26}$$

where t_0 is the starting time instant of the integration, t is the final time instant of the integration, $\boldsymbol{x}_0$ denotes the initial particle positions, $\boldsymbol{\omega}(\boldsymbol{x}, s)$ is the instantaneous vorticity distribution, $\boldsymbol{x}(s;\boldsymbol{x}_0)$ denotes the instantaneous particle positions, s is the variable of integration, and $\overline{\boldsymbol{\omega}}(s)$ is the spatial mean of the vorticity.

The LAVD method does not depend on an arbitrarily chosen threshold value, and a rotationally coherent Lagrangian vortex must satisfy the following conditions [22]:

1. It is an evolving material domain $D(t)$ where $D(t_0)$ is filled with tubular level surfaces of $\mathrm{LAVD}_{t_0}^{t}(\boldsymbol{x}_0)$ and the LAVD values are decreasing as one moves outwards.

2. The boundary $B(t)$ of $D(t)$ is a material surface where $B(t_0)$ is the outermost tubular level surface (minimum) of $\mathrm{LAVD}_{t_0}^{t}(\boldsymbol{x}_0)$ in $D(t_0)$.

3. The center $C(t)$ of $D(t)$ is a material set where $C(t_0)$ is the innermost member (maximum) of $\mathrm{LAVD}_{t_0}^{t}(\boldsymbol{x}_0)$ in $D(t_0)$.

During the detection, the values of three vortex detection parameters have to be set. These parameters are the following: number of contour levels intended to be extracted (Nct), minimum arc-length threshold (MinLength, %), and maximum convexity deficiency threshold (DeficiencyThresh, %). The minimum arc-length threshold is expressed as a percentage of the characteristic length of the given geometry, an idea proposed by Kovács et al. [36], because originally a general length scale had to be set which was harder to interpret for different setups ranging from atmospheric to engineering flow case studies. For instance, in the case of the cylinder geometry the characteristic length is the cylinder diameter. If MinLength is set to e.g., 30% of the cylinder diameter, then the vortices whose circumference falls below this value are neglected. The physical meaning of these parameters (Nct, MinLength, DeficiencyThresh) can be well interpreted, and they do not correspond directly to the LAVD values. The values of these parameters were set based on the findings of previous studies [36].

3 Simulation settings and results for the cylinder and the rectangular cuboid

The flow cases under investigation consist of three-dimensional simulations of flow around a cylinder and a rectangular cuboid with different Reynolds numbers and angles of attack. These geometries were chosen due to their relevance in various engineering and architectural applications, such as chimneys [37], skyscrapers [38], and bridge piers [39]. Studying the flow around these shapes provides valuable insights into vortex shedding, and flow separation, which are critical for designing structures that can withstand aerodynamic forces and maintain stability in different environmental conditions. In addition, these simple enough flows are a convenient benchmark problem for testing vortex detection methods.

3.1 Geometrical model

Three different geometrical models (cylinder, rectangular cuboid with 0° and 45° angles of incidence) were constructed in the Ansys SpaceClaim software. The dimensionless coordinates bounding the fluid domain are the following: $-20 < x/d < 40$, $-20 < y/d < 20$, and $0 < z/d < 6$. Where d is the characteristic length of the given geometry. The characteristic length is the diameter of the cylinder (D), and the side length of the square (h) for the cylinder and the rectangular cuboid geometries, respectively ($D = h = 0.01\,\mathrm{m}$).

3.2 Meshing of the flow field

Structured meshes, consisting of hexahedral elements only, were created with the Ansys Workbench Mesher software. A representative example can be seen in Fig. 3.1 (there are 30 cells in the z-wise direction).

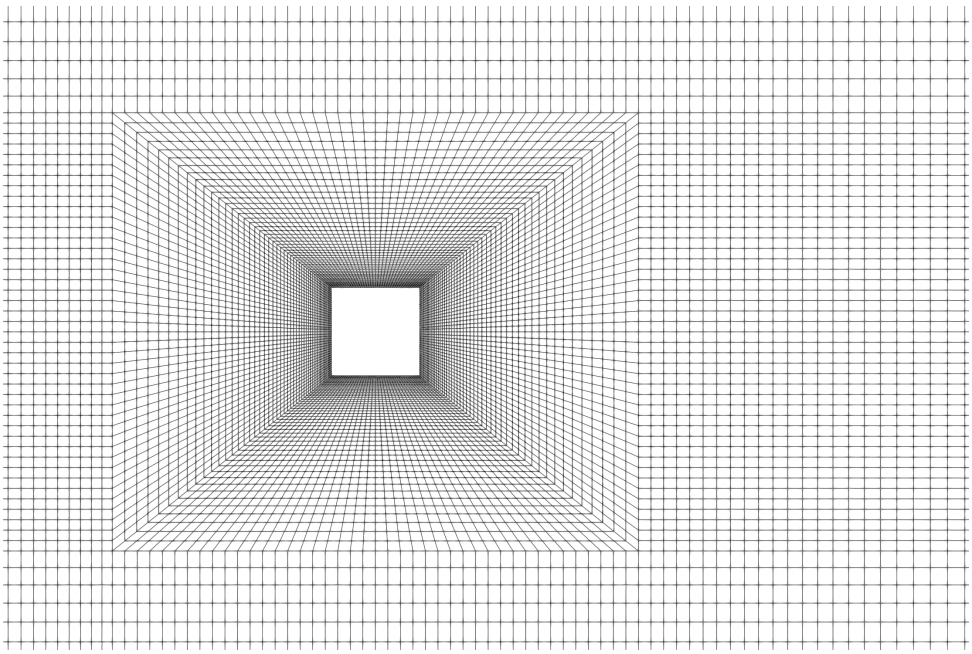

Figure 3.1: Local mesh (rectangular cuboid, $\theta = 0°$, $x - y$ plane).

In order to check the quality of the generated grids, the maximum skewness values were examined, and for all cases they were below 0.6 which is satisfactory. In addition, mesh inde-

pendence studies were also conducted. Three grids with different cell count, but same structure were created (coarse, medium, fine), and the monitored field variables were the time-averaged drag coefficient, and the root-mean-square (RMS) value of the lift coefficient. With the help of the Richardson extrapolation the measured orders of convergence, the discretization errors, and the (exact) values extrapolated to the infinitely fine mesh were also determined. The results of the mesh independence study can be seen in Fig. 3.2, where N denotes the number of cells, and $\overline{c}_D$, and $c_{L,\mathrm{RMS}}$ denote the time-averaged drag coefficient, and the RMS value of the lift coefficient, respectively. The $1/N \to 0$ case corresponds to the $\overline{c}_D$, and $c_{L,\mathrm{RMS}}$ values extrapolated to the infinitely fine mesh. From the results it was concluded that by using the medium meshes (cell count: 909,000) in each case, accurate simulation results can be obtained.

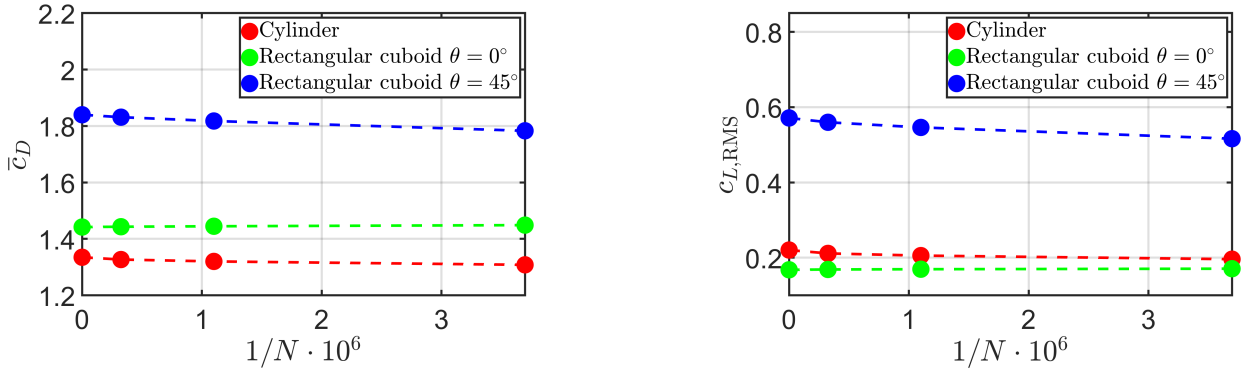

(a) Drag coefficient results.

(b) Lift coefficient results.

Figure 3.2: Mesh independence study.

3.3 Simulation settings and validation of the results

Five different transient simulations were run with the Ansys Fluent software. The different cases can be seen in Table 3.1. In the table θ [°] denotes the angle of incidence, and Re is the Reynolds number. The Reynolds numbers were chosen based on the occurrence of coherent vortex rows, thus making vortex detection more straightforward. The applied model was the *Viscous Laminar* model, and the air was assumed to be incompressible ideal gas ($\varrho = 1.225\,\mathrm{kg/m^3}$, $\mu = 1.7894 \cdot 10^{-5}\,\mathrm{kg/(m \cdot s)}$). SIMPLE pressure-velocity coupling was used, and second-order upwinding was set for the numerical schemes. For the inlet a velocity inlet, and for the outlet a pressure outlet boundary condition were prescribed. No-slip boundary condition was set for the cylinder surface. At the lower and upper boundaries symmetry boundary conditions were used, and a periodic boundary condition was prescribed in the spanwise direction. The applied boundary conditions can be seen in Fig. 3.3.

Table 3.1: Simulation cases.

Geometry	θ [°]	Re
cylinder	-	60
	-	100
rectangular cuboid	0	100
	0	140
	45	120

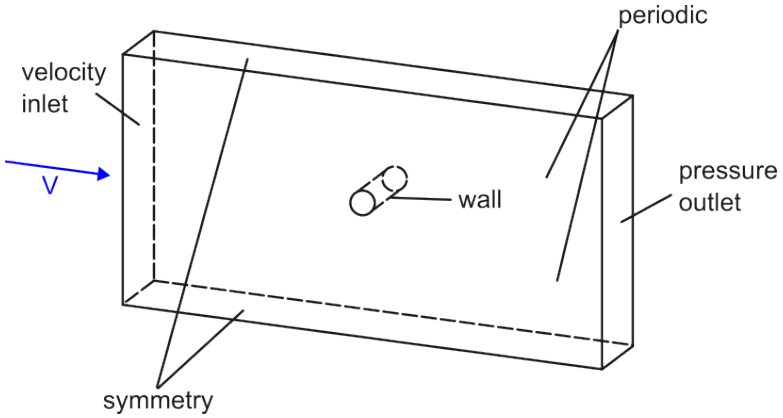

Figure 3.3: The applied boundary conditions.

In each simulation case symmetric, periodic vortex shedding could be observed which is characteristic of the widely known *von Karman vortex street* phenomenon. In Fig. 3.4 the contour plot of the velocity magnitude at a given $x-y$ plane can be seen for one of the cases. For the validation of the simulation results the time-averaged drag coefficient, the RMS value of the lift coefficient, and the Strouhal number were inspected, and compared with the literature data [40, 41], this can be seen in Table 3.2. In the table θ [°] denotes the angle of incidence, Re is the Reynolds number, $c_{L,\mathrm{RMS}}$ is the RMS value of the lift coefficient, $\overline{c}_D$ is the time-averaged value of the drag coefficient, and St is the Strouhal number. The subscripts 'sim' and 'lit' denote the simulation results, and the literature data, respectively. It can be seen that the simulation results are in great accordance with the literature data.

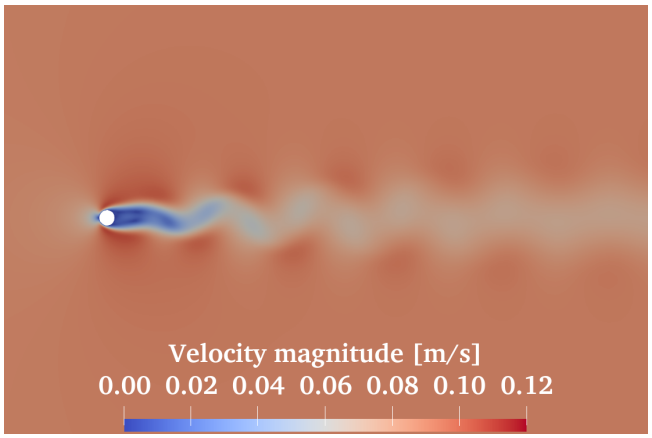

Figure 3.4: Contour plot of the velocity magnitude at a given $x-y$ plane (Re = 60, cylinder).

Table 3.2: Comparison of the simulation results with the literature data.

Geometry	θ [°]	Re	$c_{L,\mathrm{RMS,sim}}$	$c_{L,\mathrm{RMS,lit}}$	$\overline{c}_{D,sim}$	$\overline{c}_{D,\mathrm{lit}}$	$\mathrm{St}_{\mathrm{sim}}$	$\mathrm{St}_{\mathrm{lit}}$
cylinder	-	60	0.08	0.09	1.39	1.38	0.13	0.14
	-	100	0.21	0.22	1.32	1.32	0.16	0.16
rectangular cuboid	0	100	0.17	0.17	1.44	1.43	0.14	0.14
	0	140	0.24	0.25	1.43	1.39	0.15	0.16
	45	120	0.55	0.55	1.82	1.76	0.18	0.18

4 Quantitative comparison of the selected methods based on the cylinder and the rectangular cuboid simulations

In the current section the comparison of the selected detection methods is performed. The ω-criterion, Q-criterion, λ_2-criterion, Ω-method, the Rortex-, and the Omega-Liutex methods were implemented in Matlab based on the relevant publications. For the LAVD method a freely accessible Matlab code, provided by Haller et al. [22], was rewritten so that it could be used for scattered data, because the original code was meant to be used for equidistant, uniform grid data, which is rarely available.

For the comparison, the different detection results are displayed along with the chosen threshold values. Moreover, in order to *quantify the accuracy* (with respect to a selected method) of the detection results, four different classification metrics are used. These are the following [42]:

$$A = \frac{TP + TN}{TP + TN + FP + FN}, \tag{4.1}$$

$$P = \frac{TP}{TP + FP}, \tag{4.2}$$

$$R = \frac{TP}{TP + FN}, \tag{4.3}$$

$$F1 = \frac{2 \cdot P \cdot R}{P + R}, \tag{4.4}$$

where: A is accuracy, P is precision, R is recall, *F1* is F1 score, and *TP*, *TN*, *FP*, *FN* denote the numbers of true positive, true negative, false positive, and false negative data, respectively. Accuracy is the proportion of all correct predictions out of the total number of predictions. Precision means that out of the positive predictions how many were true, and recall means that out of the data points that should be predicted as true how many were correctly predicted. At last, the F1 score combines precision and recall, and this is the most descriptive out of these four classification metrics. Through the calculation of these metrics it is also possible to display how the different threshold values affect the detection results.

For the calculation of the above-described metrics a benchmark method had to be chosen, with which the other detection results can be compared. This benchmark method was chosen to be the LAVD method, because as it was stated in *Section 1* the author agrees with the LAVD-based vortex definition (very vaguely vortices are a region of the flow in which material elements experience the same rotation).

4.1 Comparison of the results on a selected test case (Re = 60, cylinder)

The following steps outline the process for the comparison based on the classification metrics:

1. Performing the vortex detection with the LAVD method, and selecting the regions as points which lie within the detected vortex boundaries.

2. Performing the vortex detection with the other selected methods for various threshold values, and selecting the detected regions (as points).

3. Determining the number of *TP*, *TN*, *FP*, and *FN* data.

4. Calculating the classification metrics (accuracy, precision, recall, F1 score) for each case.

For the ω-criterion, Q-criterion, and the Rortex method the threshold values can be chosen within the interval of $(0; \infty)$. For the λ_2-criterion this interval is $(-\infty; 0)$. Thus, making an initial guess for the threshold value is a challenge for these methods. As for the Ω-method, and the Omega-Liutex method the interval to choose from is restricted to $(0; 1)$, because these quantities are normalized.

In Fig. 4.1 the accuracy, precision, recall, and F1 score values can be seen as a function of the chosen isovalues for the different detection methods (cylinder, $\mathrm{Re} = 60$), and in Fig. 4.2 the comparison of the different vortex detection results with the LAVD method can be seen (the LAVD results are denoted by dark blue dots in each figure, and the light blue isosurfaces denote the results obtained by the methods named in the subcaptions). By looking at the tendency of the F1 score (this is the most descriptive out of the four metrics) it can be observed that for the vorticity it has a maximum value at $\omega_{\mathrm{iso}} = 0.5$ 1/s. In the case of the other methods the F1 score decreases as the absolute values of the threshold values are increased, and it does not have a maximum value. Meaning, the most accurate results can be obtained by setting the threshold values close to zero (for this low Reynolds number case).

With respect to the accuracy, the λ_2-criterion had the highest overall value (for $\lambda_{2,\mathrm{iso}} = -0.025$ 1/s^2), and with respect to the precision the Rortex method achieved the highest overall result (for $R_{\mathrm{iso}} = 0.4$ 1/s). The ω-criterion gave the highest values for the recall (for $\omega_{\mathrm{iso}} = 0.025 - 0.3$ 1/s), and the F1 scores (for $\omega_{\mathrm{iso}} = 0.5$ 1/s). It is observable that for the ω-criterion, Q-criterion, λ_2-criterion, and the Rortex method the results are highly influenced by the chosen isovalues, which isovalues are already in the vicinity of the *optimal* values for the current case. If the threshold values are not close to the optimal value, then the obtained results are highly inaccurate. As for the Ω-method, and the Omega-Liutex method it can be seen that the results are indeed insensitive to moderate threshold changes near the empirical 0.52 value, and these methods also seem to provide relatively reliable results. In Table 4.1 the sensitivity of the different methods (presenting the absolute differences in the F1 scores, because as it was stated beforehand this metric is the most descriptive) to given threshold changes can be seen.

Table 4.1: Sensitivity of the methods to threshold changes ($\mathrm{Re} = 60$, cylinder).

	Isovalue 1	Isovalue 2	$\lvert\Delta_{\mathrm{iso}}\rvert$ (%)	$\lvert\Delta_{\mathrm{F1}}\rvert$ (%)
ω-criterion	0.5	1	50	32
Q-criterion	0.5	1	50	64
λ_2-criterion	-0.5	-1	50	64
Ω-method	0.45	0.56	20	18
Rortex method	0.5	1	50	52
Omega-Liutex method	0.45	0.56	20	19

By examining Fig. 4.2 it is observable that the ω-criterion obtained the highest recall value (which expresses that out of the data points that should be predicted as true how many were correctly predicted) because it significantly overpredicted the vortical domain. Each method (except for the LAVD method) detected the boundary layer near the cylinder as a vortical domain (as can be seen in Fig. 4.2), and these regions could not be eliminated by changing the threshold values. For the ω-criterion this is not surprising, since as it was stated above this method is not able to distinguish between shear layers and the actual swirling motion of the vortex. The Q-criterion, λ_2-criterion, and the Ω-method can also be contaminated by shear [32].

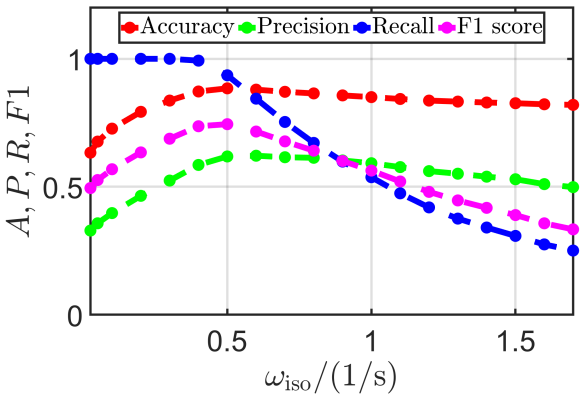

(a) ω-criterion.

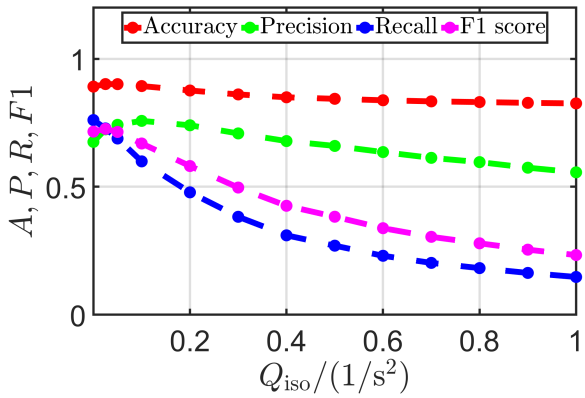

(b) Q-criterion.

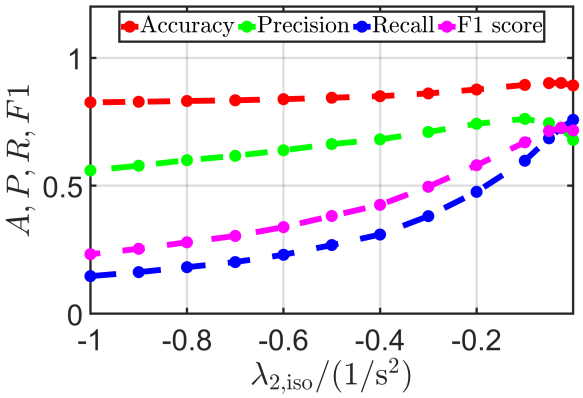

(c) λ_2-criterion.

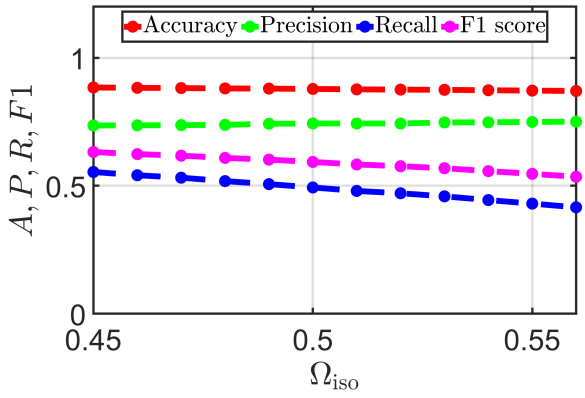

(d) Ω-method.

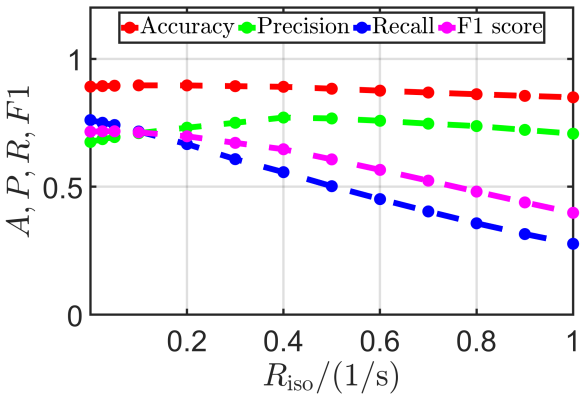

(e) Rortex method.

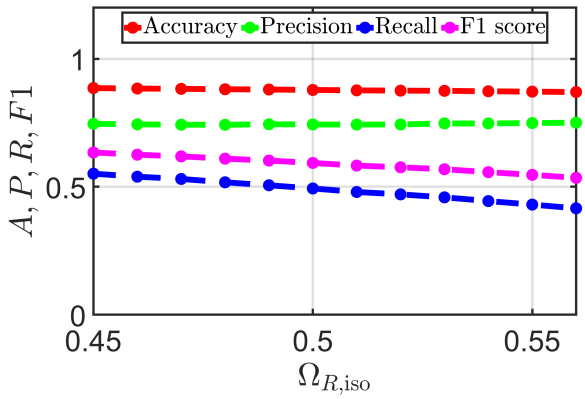

(f) Omega-Liutex method.

Figure 4.1: Metrics as a function of the isovalues (Re = 60, cylinder).

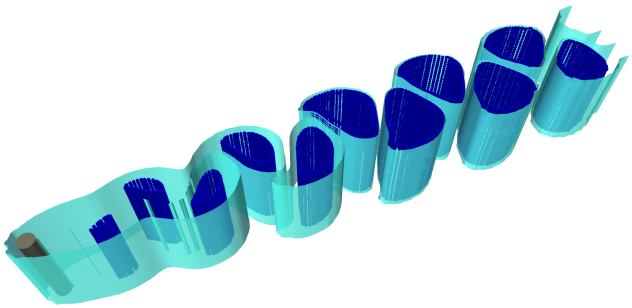

(a) ω-criterion ($\omega_{\text{iso}} = 0.35$ 1/s).

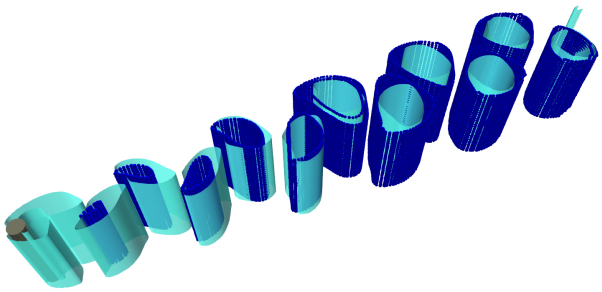

(b) Q-criterion ($Q_{\text{iso}} = 0.1$ 1/s^2).

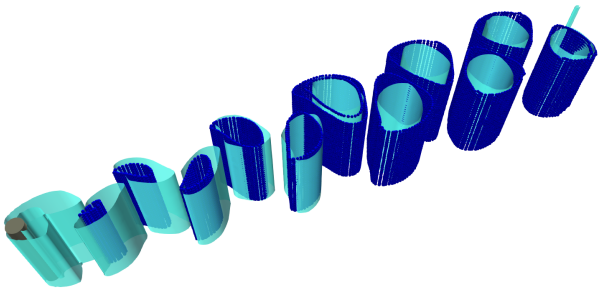

(c) λ_2-criterion ($\lambda_{2,\text{iso}} = -0.1$ 1/s^2).

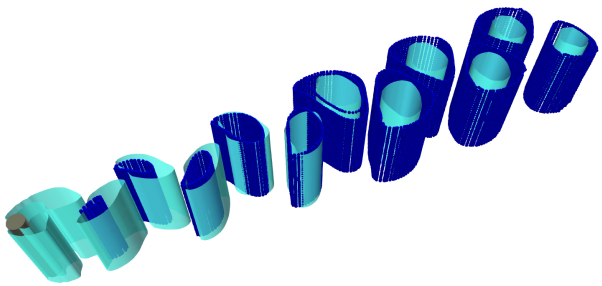

(d) Ω-method ($\Omega_{\text{iso}} = 0.52$).

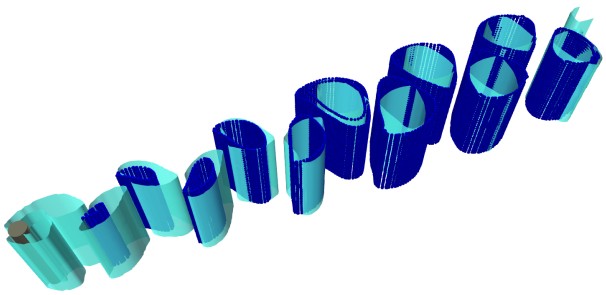

(e) Rortex method ($R_{\text{iso}} = 0.3$ 1/s).

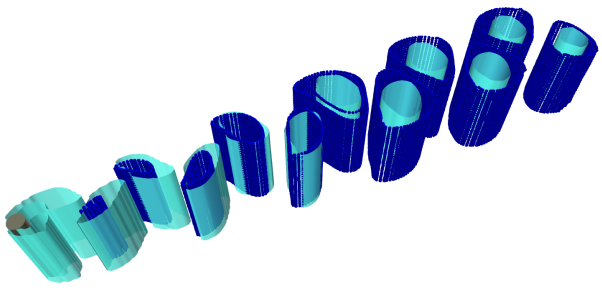

(f) Omega-Liutex method ($\Omega_{R,\text{iso}} = 0.52$).

Figure 4.2: Comparison of vortex detection results (Re = 60, cylinder). The LAVD results are denoted by the dark blue dots.

The surprising result was that both the Rortex method and Omega-Liutex method failed in this sense too, because it was highly emphasized that these methods are the only ones without the possibility of shear contamination [32]. The LAVD method did not detect the regions touching the cylinder surface, however, for lower MinLength values this method detected the regions in front of the cylinder as vortical domains as can be seen in Fig. 4.3b. For properly adjusted MinLength values (e.g, Minlength = 150%), which are in accordance with the values suggested by Kovács et al. [36], the method did not detect the region in front of the cylinder (see Fig. 4.3a). In Fig. 4.3 the contour plot of the LAVD values can be seen in a given $x - y$ plane. The red dots denote the centers, and the red closed curves denote the boundaries of the vortices. From the results it can be concluded that the LAVD method is robust in distinguishing between actual vortical structures and regions of high shear.

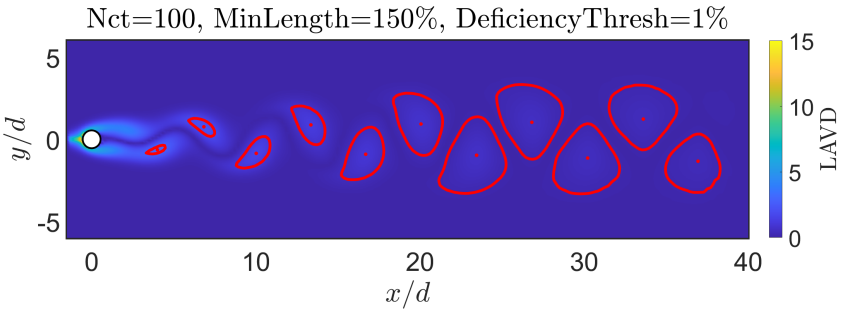

(a) LAVD results (Re = 60, cylinder) with a proper MinLength parameter ($z/d = 3$).

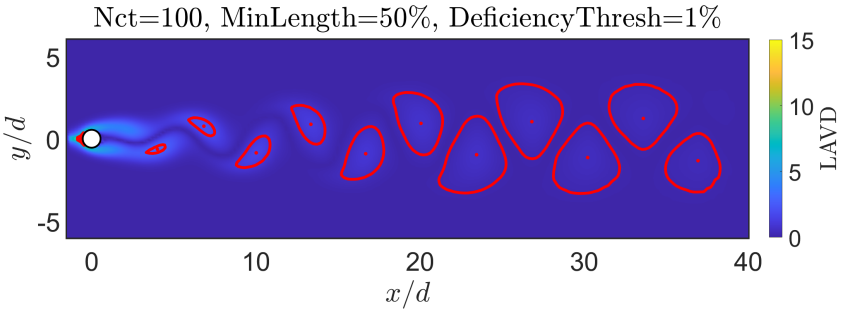

(b) LAVD results (Re = 60, cylinder) with an improper MinLength parameter ($z/d = 3$).

Figure 4.3: LAVD results in a given $x - y$ plane.

4.2 Testing the methods for the other simulation cases

The determination of the classification metrics for the different isovalues, and the vortex identification were performed for the other simulation cases as well. One of the cases (Re = 100, cylinder) is presented in the current section (the rest of the figures for the other cases can be found in the *Appendix*). In Fig. 4.4 the accuracy, precision, recall, and F1 score values can be seen as a function of the chosen isovalues for the different detection methods (cylinder, Re = 100), and in Fig. 4.5 the comparison of the different vortex detection results with the LAVD method can be seen (the LAVD results are denoted by dark blue dots in each figure).

With respect to the F1 score, contrary to the previous case, the Q-criterion, λ_2-criterion, and the Rortex method results also have maximum values (apart from the ω-criterion), but these threshold values are also close to zero similarly to the previous case. The general tendency of the curves is similar to the previous case, and this is true for the other cases as well. Based on all of the simulation results it can be concluded that for these low Reynolds number cases the optimal threshold values (for these methods) are close to zero. However, for example Balla et al. [9] performed vortex detection with the Q-criterion on the numerical simulation of tip leakage flow of a low-speed axial fan for a higher Reynolds number of 105,000. For this case the applied isovalue with respect to the Q-criterion was $3 \cdot 10^6$ 1/s^2. This significant difference in the optimal threshold values further strengthens that the appropriate isovalues for these methods are highly dependent on the specific flow conditions, thus making it harder to perform accurate vortex detection.

The sensitivity of the F1 scores were determined, this can be seen in Table 4.2 (the rest of the figures for the other cases can be found in the *Appendix*). It can be seen from this table that in this case the ω, Q, λ_2, and the Rortex results are not that sensitive to the threshold

changes, however, it should be noted that the sensitivity was high for the previous case, and these results are the best possible results that can be obtained with these methods. On the other hand, from the results it can be seen that the Ω- and the Omega-Liutex methods can indeed provide relatively accurate results with low sensitivity (the change is $16-19\%$ in the F1 scores in each simulation case) to moderate threshold changes for each case (as can be seen from the tables in the *Appendix*).

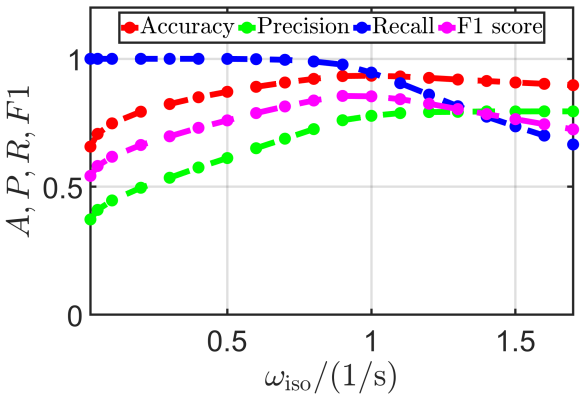

(a) ω-criterion.

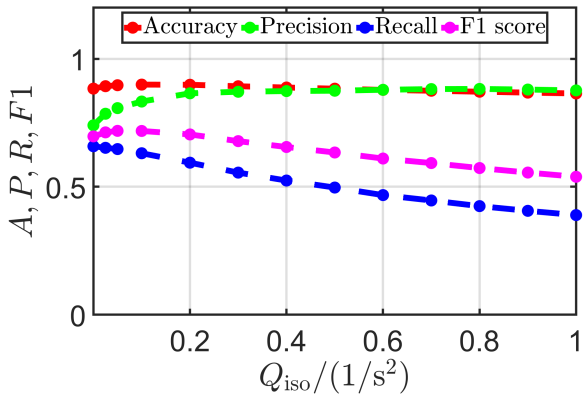

(b) Q-criterion.

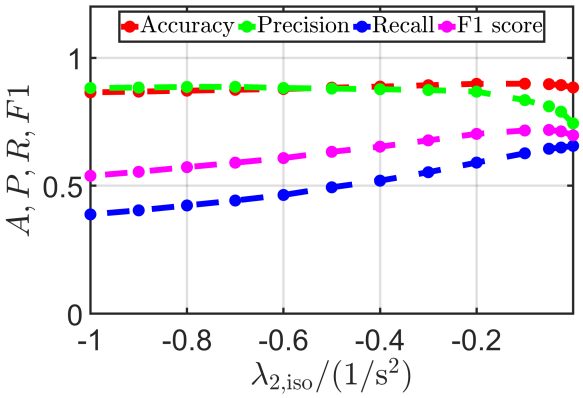

(c) λ_2-criterion.

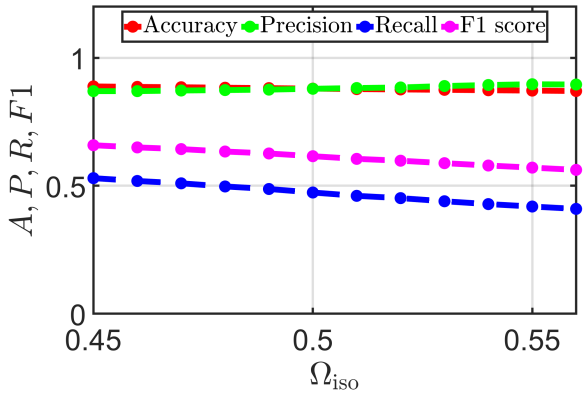

(d) Ω-method.

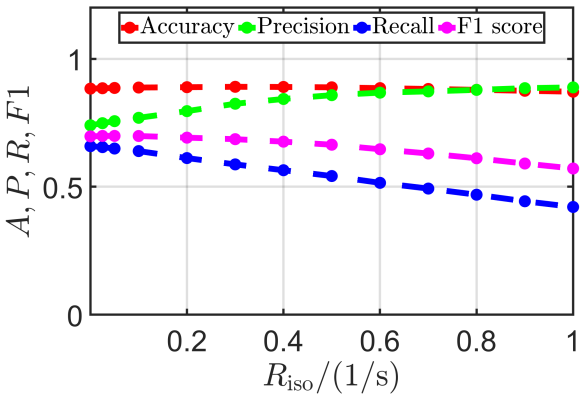

(e) Rortex method.

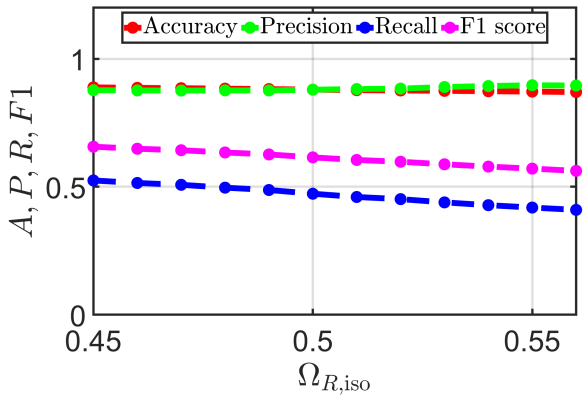

(f) Omega-Liutex method.

Figure 4.4: Metrics as a function of the isovalues (Re = 100, cylinder).

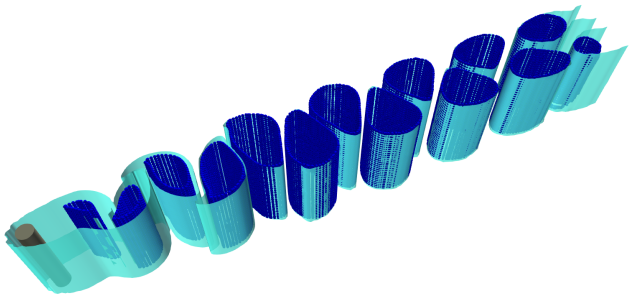

(a) ω-criterion ($\omega_{\text{iso}} = 0.9$ 1/s).

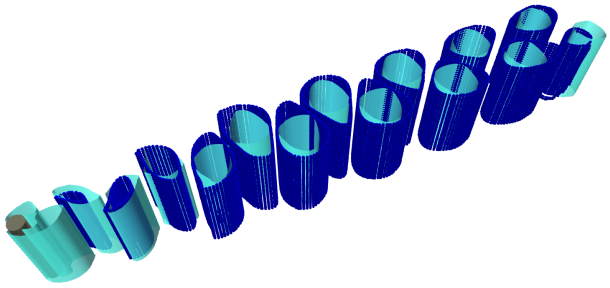

(b) Q-criterion ($Q_{\text{iso}} = 0.3$ 1/s^2).

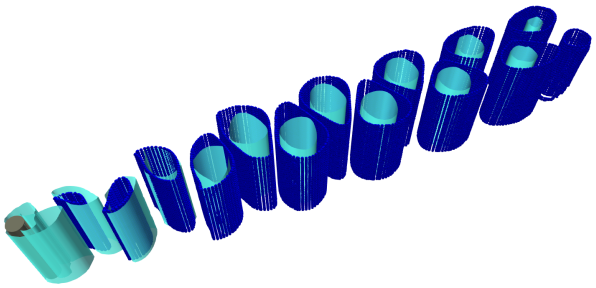

(c) λ_2-criterion ($\lambda_{2,\text{iso}} = -1$ 1/s^2).

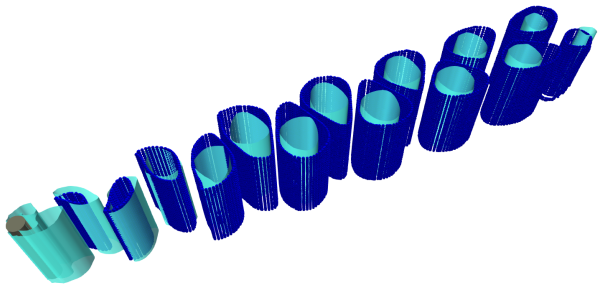

(d) Ω-method ($\Omega_{\text{iso}} = 0.52$).

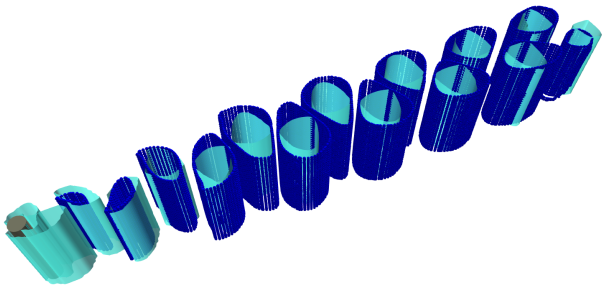

(e) Rortex method ($R_{\text{iso}} = 0.7$ 1/s).

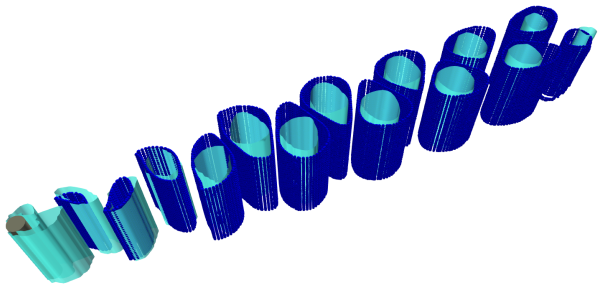

(f) Omega-Liutex method ($\Omega_{R,\text{iso}} = 0.52$).

Figure 4.5: Comparison of vortex detection results (Re = 100, cylinder). The LAVD results are denoted by the dark blue dots.

Table 4.2: Sensitivity of the methods to threshold changes (Re = 100, cylinder).

	Isovalue 1	Isovalue 2	$\lvert\Delta_{\text{iso}}\rvert$ (%)	$\lvert\Delta_{\text{F1}}\rvert$ (%)
ω-criterion	0.5	1	50	11
Q-criterion	0.5	1	50	18
λ_2-criterion	-0.5	-1	50	17
Ω-method	0.45	0.56	20	17
Rortex method	0.5	1	50	16
Omega-Liutex method	0.45	0.56	20	17

Based on previous studies and on the current findings important characteristics of the applied detection methods are summarized in Table 4.3. In the table 'negl.' means negligible, and 'sign.' means significant.

Table 4.3: Characteristics of the applied vortex identification methods.

Method	Objective/ Galilean invariant	Can be contaminated by shear	Depends on an arbitrary threshold	Running time	Implementation complexity	Sensitivity to parameter changes
ω	none	yes	yes	negl.	easy	high
Q	Galilean	yes	yes	negl.	easy	high
λ_2	Galilean	yes	yes	negl.	easy	high
Ω	Galilean	yes	yes	negl.	easy	low
Rortex	Galilean	yes (based on experience)	yes	negl.	moderate	high
Omega-Liutex	Galilean	yes (based on experience)	yes	negl.	moderate	low
LAVD	objective	no, if MinLength is set correctly	no	sign.	hard	low

The following additional comments with respect to Table 4.3 can be made:

1. It was possible only for the LAVD method to eliminate the shear contamination through the adjustment of the MinLength parameter.

2. The LAVD method does not depend on an arbitrary threshold value with respect to the field itself. However, it does depend on three vortex detection parameters. These values correspond to the geometry of the vortices, thus the physical meaning is clear. Based on previous studies [36] the proper adjustment of these parameters is relatively easy to perform.

3. With the LAVD method it is possible to obtain both the centres and the boundaries of the vortices.

4. The main drawback of the LAVD method is the long running time. Using 10 time steps, the running of the code took approximately 2 hours in Matlab while utilizing 1 Intel® Core™ i5-12500H processor core with 2.50 GHz base frequency. The other methods only use 1 time step, and they depend on the instantaneous velocity field. It is important to mention that the LAVD method is the only Lagrangian method out of the examined ones. There are also Lagrangian methods, derived from material coherence, that are easier to compute and do not require a dense set of initial conditions, such as the trajectory rotation angle (TRA) proposed by Haller et al. [43]. Testing additional Lagrangian methods is the subject of future research.

5. The Rortex method seems to perform well (except for the shear contamination), and it can also give the direction of the rotation, and the rotation strength, however, it depends on an arbitrary threshold value. The Ω-method, and the Omega-Liutex method provided relatively accurate results (compared to the LAVD method) by setting the threshold values close to the empirical 0.52 value, and they are also insensitive to moderate threshold changes. As it was mentioned beforehand, by changing the threshold values in the 0.45-0.56 range the change was 16-19 % in the F1 scores in each simulation case.

5 Testing the methods on a circular arc cambered plate profile

5.1 Introduction to cambered plates

Circular arc cambered plate profiles are often applied in low-speed axial flow fans [15, 16] due to their relatively low manufacturing cost and simple manufacturing technique. Apart from the aforementioned benefits, at moderate Reynolds numbers, cambered plate blades of circular arc camber line are aerodynamically competitive with or even superior to thicker airfoil profiles [44]. Both for airfoils and plate profiles, the lift coefficient gently decreases with decreasing Re. As Re decreases, the drag coefficient of airfoil profiles increases significantly; such undesired effect, however, is avoided in the case of cambered plates. Therefore, cambered plates can offer better lift-to-drag ratio than thicker profiles of comparable lift at moderate Reynolds numbers. Such benefit is expected in the order of magnitude and below of $\mathrm{Re}_c = 10^5$ [45]. In addition to ventilating or air technical fans, such advantages widen the application area of cambered plate blades towards rotors for e.g., unmanned micro air vehicles such as drones and helicopters [45, 46, 47, 48].

The shedding of rows of coherent vortices from the blades of low-speed axial flow rotors – denoted herein as profile vortex shedding (PVS) – can be a significant source of self-noise and vibration of the blades [49, 50, 51]. The PVS phenomenon, as well as its practical effects, are thoroughly detailed in the literature [7, 52, 53, 54, 55, 56, 57]. Although numerous studies have explored the causes of trailing-edge noise in airfoils operating in low Reynolds number flow regimes, the acoustic community has yet to reach a consensus on the specific cause of tonal trailing-edge noise [58].

In general, the PVS phenomenon occurs farther upstream of the trailing edge (TE), and is related to the following feedback mechanism. A separation bubble develops upstream of the TE, being the consequence of the separation and consecutive reattachment of the initially laminar blade boundary layer. The separation bubble promotes the laminar-to-turbulent boundary layer transition close to the TE. The transition is associated with instability waves propagating downstream traversing and interacting with the TE. Such interaction results in perturbations in the flow field, providing feedback toward the upstream region, and amplifying the boundary layer instabilities. The feedback loop is getting closed at a frequency being equal to the frequency of generation of boundary layer instability, i.e., at the vortex shedding frequency f. The mentioned studies [7, 52, 53, 54, 55, 56, 57] are confined to symmetric airfoil profiles being of limited relevance in low-speed fan or drone rotor applications, e.g., airfoil profiles out of NACA00 series.

Hot wire measurements on the PVS phenomenon related to a low-speed circular arc cambered plate of 8% relative camber as well as on a RAF-6E airfoil profile – both being classical representatives for blade sections of low-speed axial flow rotors – have been reported [59, 60]. In the current study two-dimensional compressible simulations of flow around a circular arc cambered plate profile were performed for different Reynolds numbers and angles of attack.

5.2 The investigated case studies

Table 5.1 presents the investigated case studies, denoted herein as Cases 1 to 6. In the table θ [°] is the angle of incidence, U_0 [m/s] is the inlet velocity, Re_c is the chord-based Reynolds number, and Ma is the Mach number. For the cases of the three different inlet velocity values, the cambered plate of $c = 0.1\,\mathrm{m}$ was subjected to $U_0 = 9.0\,\mathrm{m/s}$, $U_0 = 10.0\,\mathrm{m/s}$, and $U_0 = 15.0\,\mathrm{m/s}$.

Out of the six Cases, Cases 1, 2, and 3 represent the ones in which PVS has experimentally been detected [59, 60]. This is indicated in the table by "Yes" comments for the "PVS/Exp." row. Within the series related to the moderate velocity of $U_0 = 9.0\,\mathrm{m/s}$, i.e., Cases $1 \to 6 \to 3$ of $\theta = 1.1° \to 2.0° \to 2.7°$, the inclusion of the intermediate CFD Case 6 aims at surveying the sensitivity of occurrence as well as PVS-capturing capability of CFD to θ settings. Within the series related to the moderate angle of $\theta = 1.1°$, i.e., Cases $1 \to 4 \to 2$ of $U_0 = 9.0\,\mathrm{m/s} \to U_0 = 10.0\,\mathrm{m/s} \to U_0 = 15.0\,\mathrm{m/s}$, incorporation of the intermediate Case 4 serves for refined CFD mapping of the sensitivity of the PVS phenomenon to Re_c adjustments. At an increased angle of $\theta = 2.7°$, Cases $3 \to 5$ of $U_0 = 9.0\,\mathrm{m/s} \to U_0 = 10.0\,\mathrm{m/s}$ serve for checking the Re_c-dependence of capability of the CFD tool to capture the PVS process. At the velocity of $U_0 = 10.0\,\mathrm{m/s}$, by Cases $4 \to 5$ of $\theta = 1.1° \to 2.7°$, the limitation in capturing the PVS phenomenon at increased angles using CFD is examined.

Though the Ma values in Table 5.1 support the adequacy of incompressibility flow condition, compressibility was enabled in the computations, for the following reason: systematic preliminary CFD trials with various settings revealed that, in the case of the cambered plate, by no means was an incompressible CFD model successful in reproducing the PVS phenomenon. This observation is an important supplement to previous CFD experiences on the RAF-6E airfoil profile [61] for which incompressible modelling was found to be sufficient for an experimentally valid reproduction of the PVS process. Such substantial differences between the cambered plate and the airfoil in PVS modelling requirements form the subject of future research.

Table 5.1: The investigated case studies.

Feature		Case 1	Case 2	Case 3	Case 4	Case 5	Case 6
θ [°]		1.1	1.1	2.7	1.1	2.7	2.0
U_0 [m/s]		9.0	15.0	9.0	10.0	10.0	9.0
$\mathrm{Re}_c/10^5$		0.60	1.00	0.60	0.67	0.67	0.60
Ma		0.026	0.034	0.026	0.029	0.029	0.026
PVS	Exp.	Yes	Yes	Yes	–	–	–
	CFD	Yes	Yes	No	Yes	No	Yes

5.3 Simulation settings

The simulations were supported by the Institute of Fluid Dynamics and Thermodynamics, Faculty of Process and Systems Engineering, Otto-von-Guericke University Magdeburg. The CFD technique has been elaborated using the Ansys Fluent software. The geometrical model was constructed in SpaceClaim, and is illustrated in Fig. 5.1. The origin of the $x - y$ plane is bound to the center of the TE.

The numerical grid around the cambered plate was developed using the Ansys Workbench Mesher software, in which a fully structured C-grid, consisting of quadrilateral elements only, was generated. The meshing of the flow field can be seen in Figs. 5.2, and 5.3. The mesh serving for the data in the present paper consists of 132,800 quadrilateral elements, and the maximum skewness value is below 0.6, thus the quality of the mesh is satisfactory. In addition, $1 < y^+ < 5$ has been guaranteed in each simulation case.

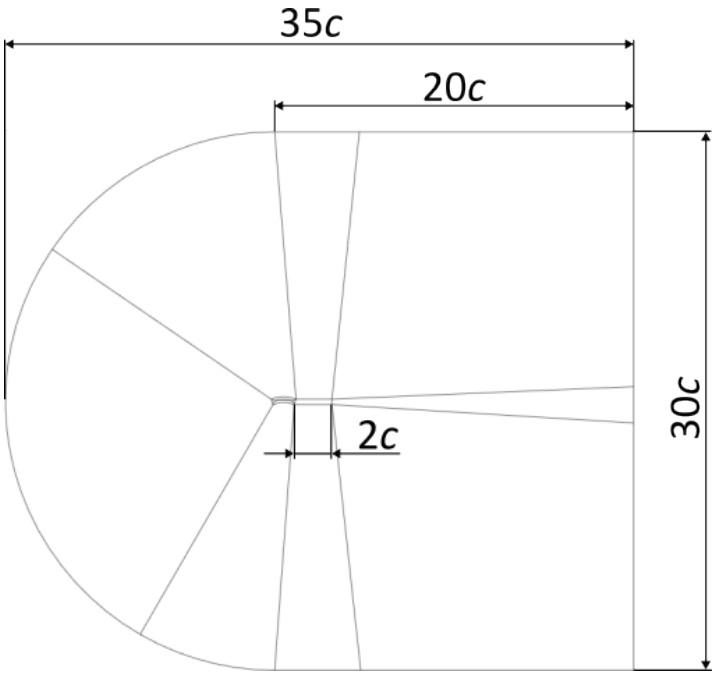

Figure 5.1: Geometrical model.

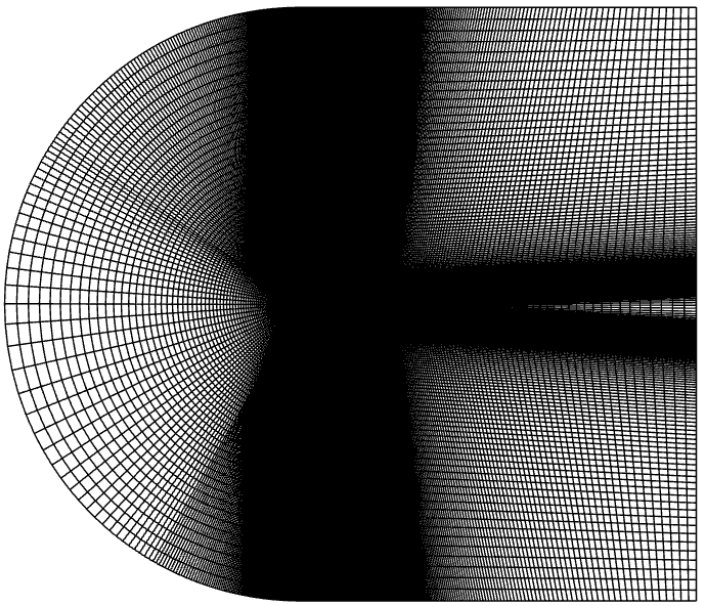

Figure 5.2: The generated C-grid.

For the simulations the Scale-Adaptive Simulation (SAS) model was used with the gamma-transport-equation for the transition model. In addition, the density-based solver was utilized, while enabling the energy equation, and employing implicit density-based formulation. The applied material was air, assuming the ideal gas law. The dynamic viscosity was set to $\mu = 1.85 \cdot 10^{-5}\,\mathrm{kg/(m \cdot s)}$. Second-order upwinding was set for the numerical schemes. For the inlet and the outlet, a pressure far field boundary condition was applied. For the boundary of the plate a no-slip wall boundary condition was set. The inlet, and outlet turbulence intensity were set to 0.8% in accordance with the measurements, with a length scale of 0.1 m. Having started with the steady-state solutions, the simulations were iterated until fully developed periodic flow solutions were achieved, enabling the capture of PVS processes.

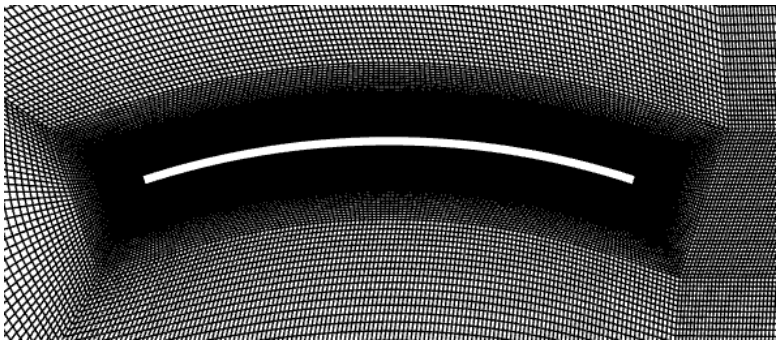

Figure 5.3: Local mesh around the cambered plate.

6 Mesh independence study

In order to evaluate the impact of grid resolution, three distinct computational grids (coarse, medium, fine) were analyzed for Case 4, and the Richardson extrapolation was applied for examining the mesh independence. The coarse, and fine meshes can be seen in Fig. 6.1. The monitored field variable was the time-averaged value of the lift coefficient.

The results with respect to the mesh independence study are shown in Table 6.1. In the table N_{c}, N_{m}, and N_{f} denote the number of cells for the coarse, medium, and fine meshes, respectively. $\overline{c}_{L,\mathrm{c}}$, $\overline{c}_{L,\mathrm{m}}$, and $\overline{c}_{L,\mathrm{f}}$ denote the time-averaged lift coefficient results for the coarse, medium, and fine meshes, and $\overline{c}_{L,\mathrm{extr}}$ denotes the lift coefficient value extrapolated to the infinitely fine mesh ($1/N \to 0$). The mesh independence results are also shown in Fig. 6.2. Based on the results, it was concluded that by utilizing the medium mesh, simulation results being sufficiently accurate for the purposes of the present paper can be obtained.

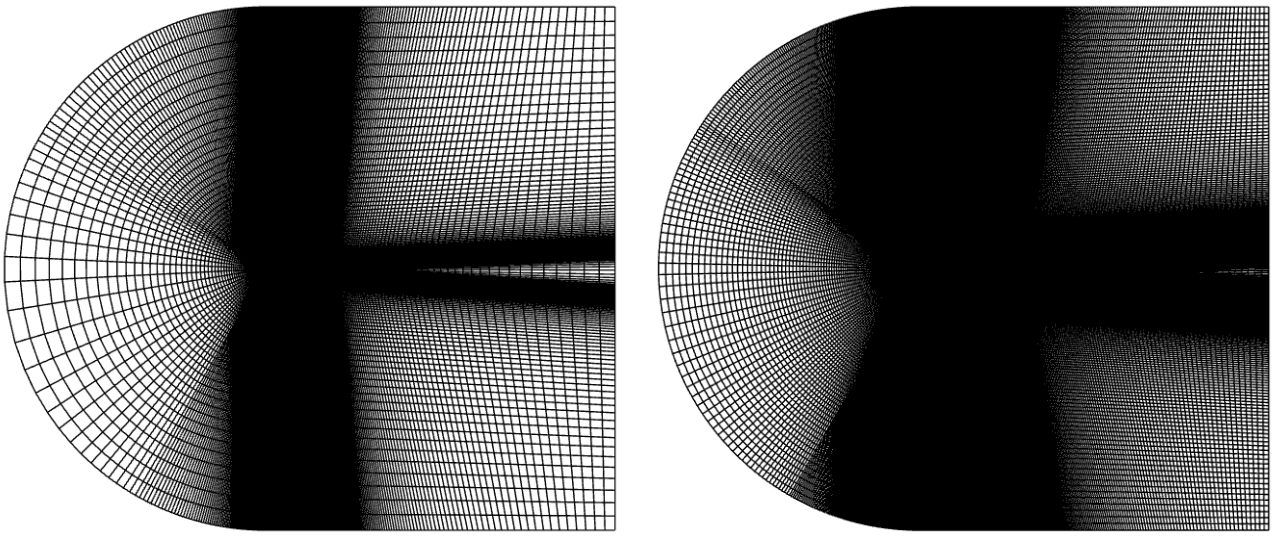

(a) Coarse grid. (b) Fine grid.

Figure 6.1: The generated grids for the mesh independe study.

Table 6.1: Results of the mesh independence study.

N_c	N_m	N_f	$\overline{c}_{L,\mathrm{c}}$	$\overline{c}_{L,\mathrm{m}}$	$\overline{c}_{L,\mathrm{f}}$	$\overline{c}_{L,\mathrm{extr}}$
59,191	132,800	298,800	0.7468	0.7712	0.7715	0.7715

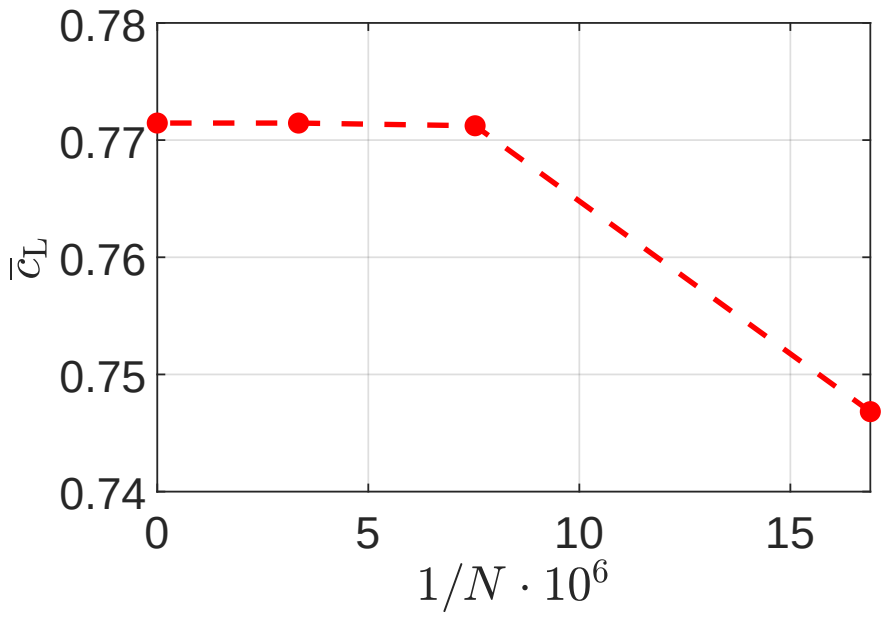

Figure 6.2: Mesh independence results.

6.1 Validation of the simulation results

The comparison of the simulation results with the measurement data [59] is presented in Table 6.2. In the table θ [°] is the angle of incidence, U_0 [m/s] is the inlet velocity, Re_c is the chord-based Reynolds number, Ma is the Mach number, c [m] is the chord length, b_t [m] is the transversal distance between the shed vortex rows, f [Hz] is the vortex shedding frequency, $\mathrm{St}^* = f \cdot b_t / U_0$ is the universal Strouhal number, $\overline{c}_L$ is the time-averaged value of the lift coefficient, PVS denotes the profile vortex shedding, Exp. and CFD denote the experimental, and the CFD-based results, respectively, and Δ_r denotes the relative error between the experimental data and the CFD results in a percentage form.

The contour plot of the velocity magnitude for Case 1, which displays the PVS phenomenon, can be seen in Fig. 6.3. Out of the six Cases, Cases 1, 2, and 3 represent the ones in which PVS has experimentally been detected [59, 60]. This is indicated in the table by "Yes" comments for the "PVS/Exp." row. Cases $1 \rightarrow 6 \rightarrow 3$ indicate that, at moderate $\mathrm{Re}_c = 0.60 \cdot 10^5$, an upper limit of $2.0° \leq \theta \leq 2.7°$ exists for the PVS-capturing capability of CFD. The contour plot of the velocity magnitude for Case 6 can be seen in Fig. 6.4. The flow field for this case is more disturbed, and the PVS phenomenon is likely to be recessed around this $\theta = 2°$ angle of incidence (in the case of CFD simulations). In Fig. 6.5 the contour plot of the velocity magnitude for Case 3 can be seen. It can be observed that the PVS phenomenon is no longer present for this case. Increasing θ to a nominal setting of $\theta = 2.7°$, the measurements at $\mathrm{Re}_c = 0.60 \cdot 10^5$ still indicated PVS, although the experimental uncertainty of $\pm 0.5°$ in angular setting [59] is also to be acknowledged. Cases $1 \rightarrow 4 \rightarrow 2$ demonstrate the CFD capability for capturing

PVS at moderate $\theta = 1.1°$ over the entire investigated $\mathrm{Re}_c = 0.60 \ldots 1.00 \cdot 10^5$ range. In the experiments [59], PVS was found to disappear for higher velocity only, i.e., $\mathrm{Re}_c = 1.40 \cdot 10^5$. As Cases $3 \rightarrow 5$ demonstrate, the lack of PVS-capturing capability of CFD at $\theta = 2.7°$ is not remediated by a moderate increase of Re_c. In Cases $5 \rightarrow 4$ of $\mathrm{Re}_c = 0.67 \cdot 10^5$, the moderation of $\theta = 2.7°$ to $\theta = 1.1°$ retains the PVS-capturing capability of CFD.

Table 6.2: Comparison of the simulation results with the mesurement data.

Feature		Case 1	Case 2	Case 3	Case 4	Case 5	Case 6
θ [°]		1.1	1.1	2.7	1.1	2.7	2.0
U_0 [m/s]		9.0	15.0	9.0	10.0	10.0	9.0
$\mathrm{Re}_c/10^5$		0.60	1.00	0.60	0.67	0.67	0.60
Ma		0.026	0.034	0.026	0.029	0.029	0.026
PVS	Exp.	Yes	Yes	Yes	–	–	–
	CFD	Yes	Yes	No	Yes	No	Yes
b_t/c	Exp.	0.055	0.057	0.055	–	–	–
	CFD	0.070	0.055	–	0.070	–	0.065
	Δ_r[%]	27	-4	–	–	–	–
f [Hz]	Exp.	310	470	290	–	–	–
	CFD	320	580	–	357	–	304
	Δ_r[%]	3	23	–	–	–	–
St*	Exp.	0.19	0.18	0.18	–	–	–
	CFD	0.25	0.21	–	0.25	–	0.22
	Δ_r[%]	32	17	–	–	–	–
$\overline{c}_L$	Exp.	0.72	0.80	0.95	–	–	–
	CFD	0.74	0.85	1.03	0.77	1.05	0.96
	Δ_r[%]	3	6	8	–	–	–

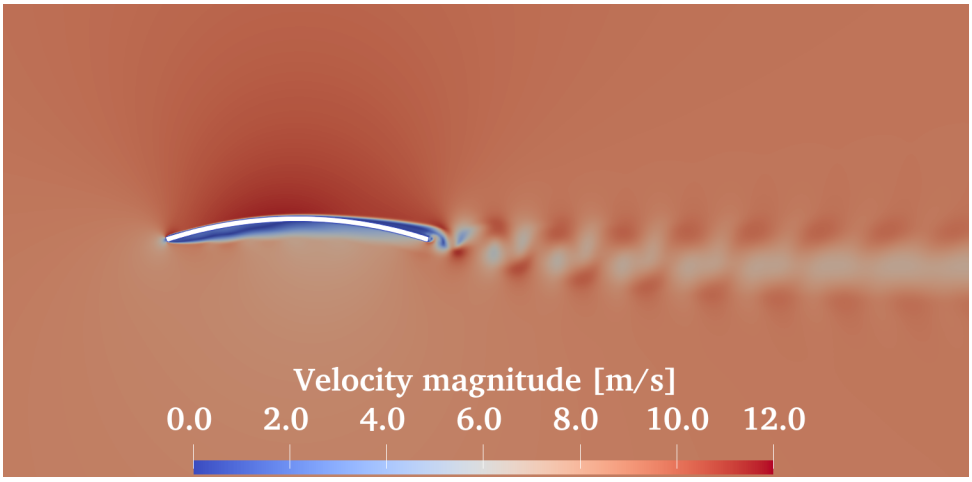

Figure 6.3: Contour plot of the velocity magnitude (Case 1).

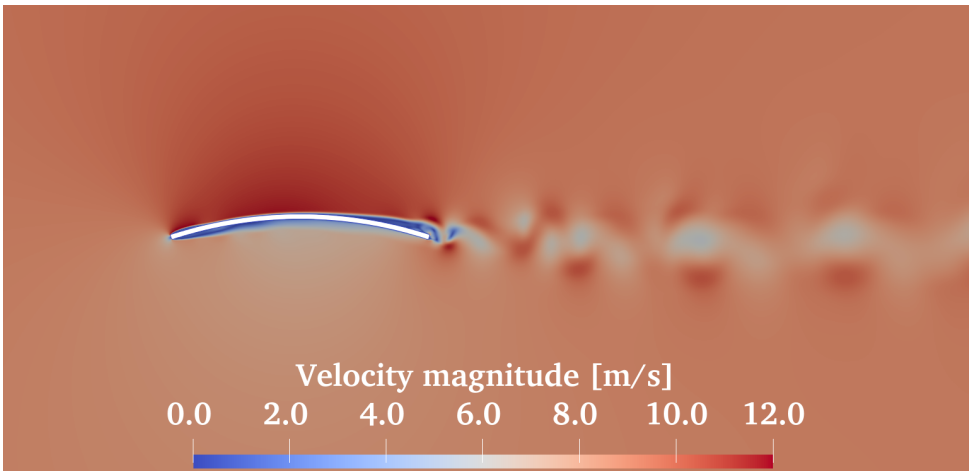

Figure 6.4: Contour plot of the velocity magnitude (Case 6).

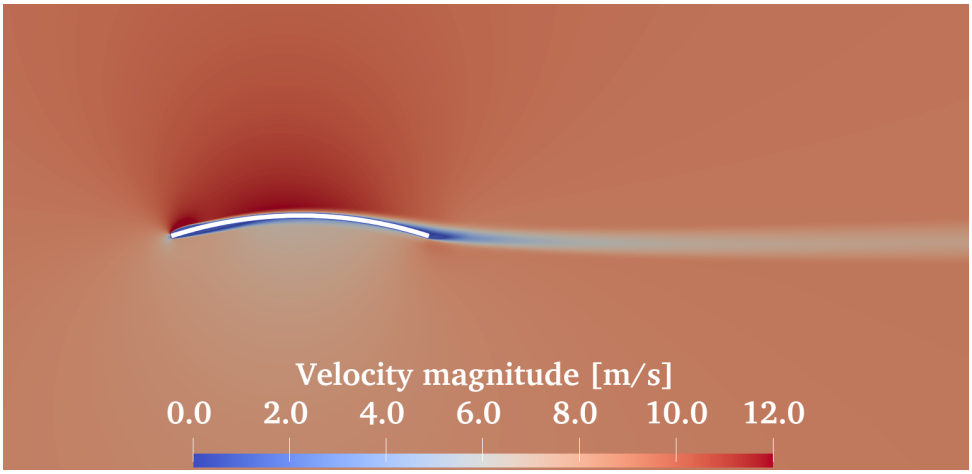

Figure 6.5: Contour plot of the velocity magnitude (Case 3).

The above discussion reveals that the occurrence of PVS for a circular arc cambered plate, demonstrated in the physical experiments [59, 60], is especially sensitive to the actual operational state of the blade section characterized by θ and Re_c. Furthermore, the CFD tool for the cambered plate exhibits limitations in PVS-capturing capability at increased θ values. Such limitations of the CFD methodology for increased θ has also been recognized in the CFD validation studies performed by Daku et al. [61].

Table 6.2 gives a comparison of the available experiment-based and CFD-based b_t, f, and St^* data. The Δ_r discrepancies are in the percent to 10 percent orders of magnitude. Based on the comparison, the CFD tool has been considered valid for testing the selected vortex detection methods for the simulation results.

6.2 Vortex detection

The two-dimensional versions of the examined detection methods were tested for one of the simulation cases presented above (Case 1). The detection results can be seen in Figs. 6.6-6.12. In Figs. 6.6-6.11 the vortical regions (denoted by the red dots) were obtained by setting given threshold values and filtering the different fields in accordance with these thresholds.

With respect to the running times, except for the LAVD method, each method's running time was negligible. The running time of the LAVD method was 170 s while utilizing 20 time steps. Based on the results it was further reinforced that the ω-, Q-, and λ_2-criteria can be contaminated by shear, as they detected the boundary layer as a vortical region near the surface of the cambered plate. In contrast, the Ω-, Rortex-, and Omega-Liutex methods performed more reliably in this context. From the current results it can be seen that they are not as prone to shear contamination as the ω-, Q-, and λ_2-criteria, but they still detected some non-vortical regions as vortices. These regions could not be eliminated through threshold adjustment without excluding actual vortices. Additionally, the results further reinfroced that the LAVD method is not prone to shear contamination (with proper parameter settings), and is capable of producing highly accurate detection results.

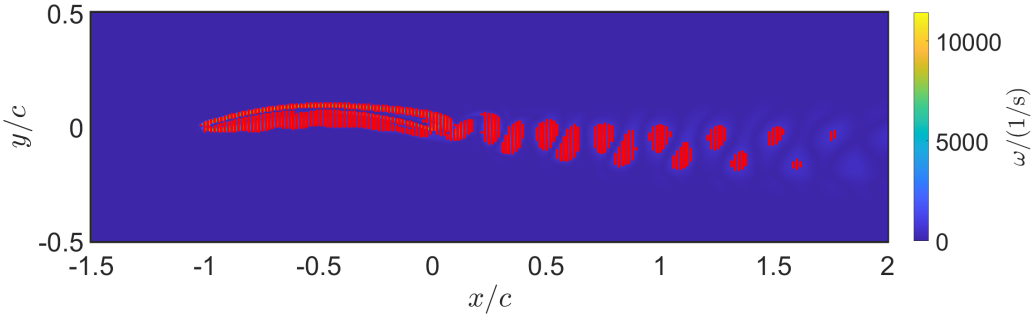

Figure 6.6: ω-criterion ($\omega_{\text{thresh}} = 500$ 1/s).

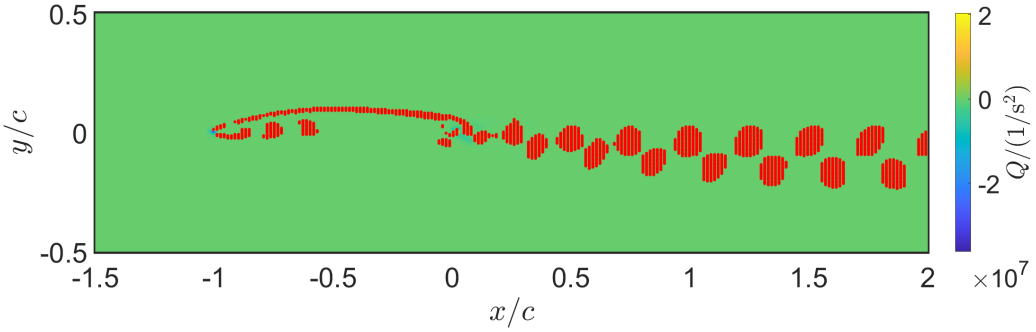

Figure 6.7: Q-criterion ($Q_{\text{thresh}} = 10^4$ 1/s^2).

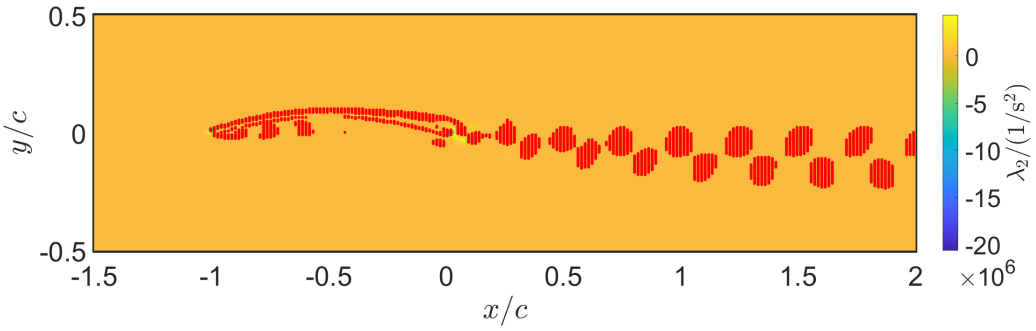

Figure 6.8: λ_2-criterion ($\lambda_{2,\text{thresh}} = -10^4$ 1/s^2).

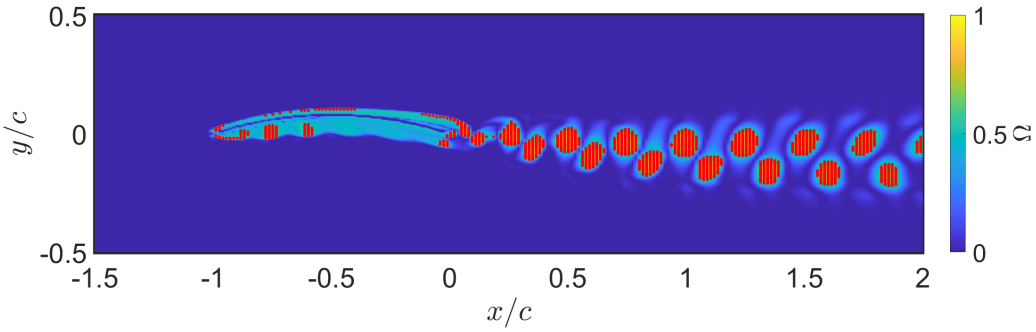

Figure 6.9: Ω-method ($\Omega_{\text{thresh}} = 0.52$).

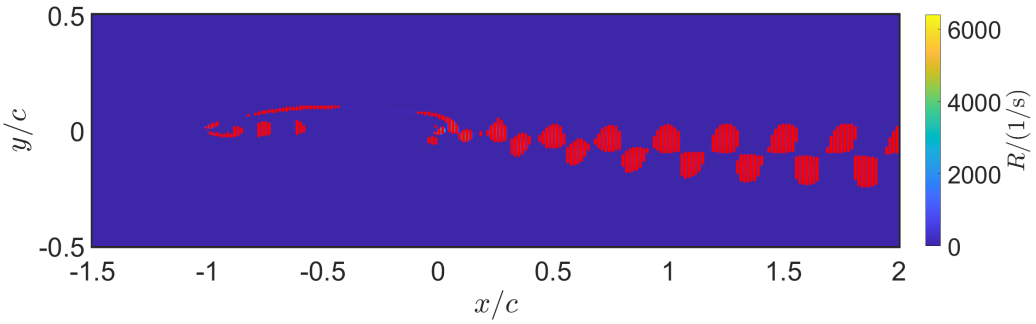

Figure 6.10: Rortex method ($R_{\text{thresh}} = 100$ 1/s).

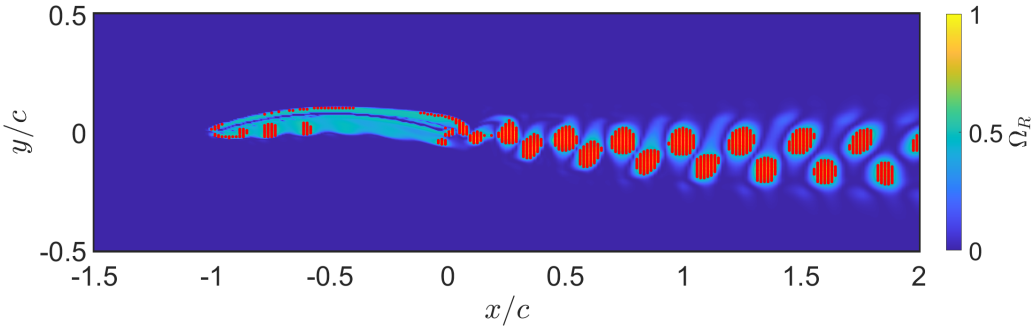

Figure 6.11: Omega-Liutex method ($\Omega_{R,\text{thresh}} = 0.52$).

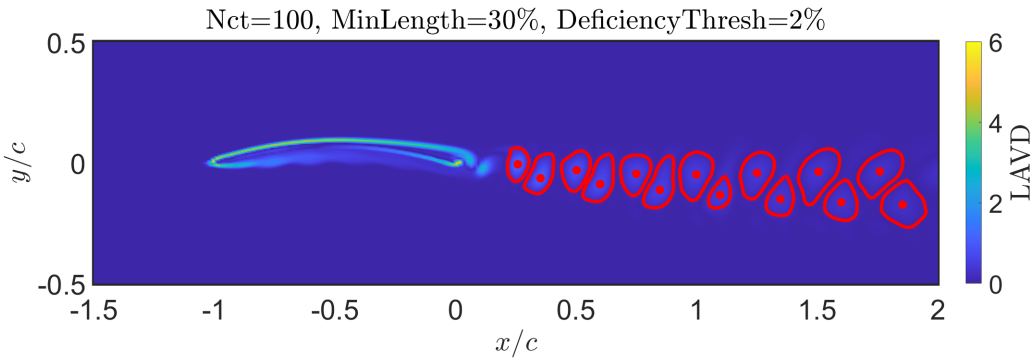

Figure 6.12: LAVD method.

7 Testing the methods on PIV measurement data

The detection methods were also tested on Particle Image Velocimetry (PIV) measurement data, because the applicability of a given detection method for imperfect velocity data (e.g., measurement data) is a very important characteristic of an ideal vortex identification method. The PIV measurements were performed by Dr. Balázs Istók and Ádám Gyurcsek at the Department of Fluid Mechanics.

PIV was used to investigate the flow field generated by a vortex cannon, specifically focusing on the interaction and collision of vortex rings. The PIV measurement employed a grid resolution of 314×194, and velocity vectors were calculated at every 8^{th} pixel. Thus the whole figure consists of 2512×1552 pixels with a spatial resolution of 14 pixels per millimeter. Images were recorded at a frequency of 300 Hz, corresponding to a time interval of 3.33 ms between consecutive image pairs, and there is an additional time interval of 150 µs between successive frames within a pair, allowing for detailed temporal resolution of the vortex ring dynamics. The measurement captured 16 time steps in total, providing a comprehensive time-resolved dataset to analyze the evolution of the vortex ring collision and flow behavior.

An animation with respect to the PIV measurements can be seen in Fig. 7.1. The detection results (corresponding to the 10^{th} frame seen in Fig. 7.1) can be seen in Figs. 7.2-7.8. For the LAVD method 7 time steps were utilized and the running of the code took 22 seconds. In addition, the MinLength parameter was non-dimensionalized by the bore diameter (50 mm) around which the vortices were generated. Similarly to the previous cases the running time of the other methods was negligible. The two methods that performed the best were the Rortex and LAVD methods. Both provided similar results in terms of accurately identifying vortex structures, with a low rate of false vortex detection. In contrast, the other methods produced a higher rate of false vortex identification. The Ω-, and the Omega-Liutex methods provided highly inaccurate results. The more thorough investigation of the applicability of vortex identification criteria to measurement data forms the subject of future research.

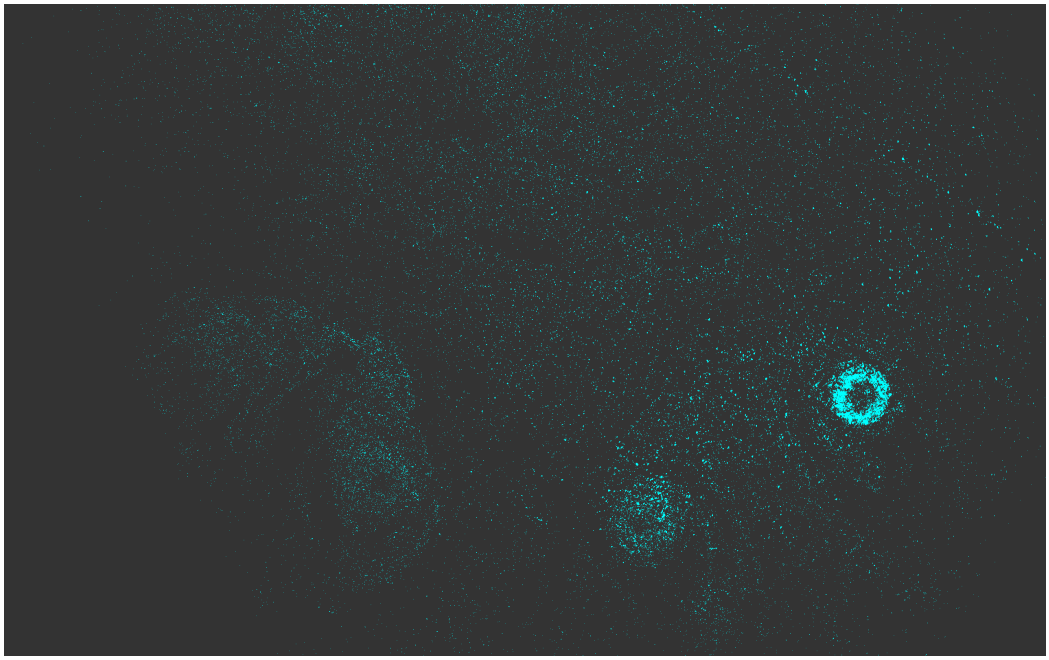

Figure 7.1: PIV measurement animation.

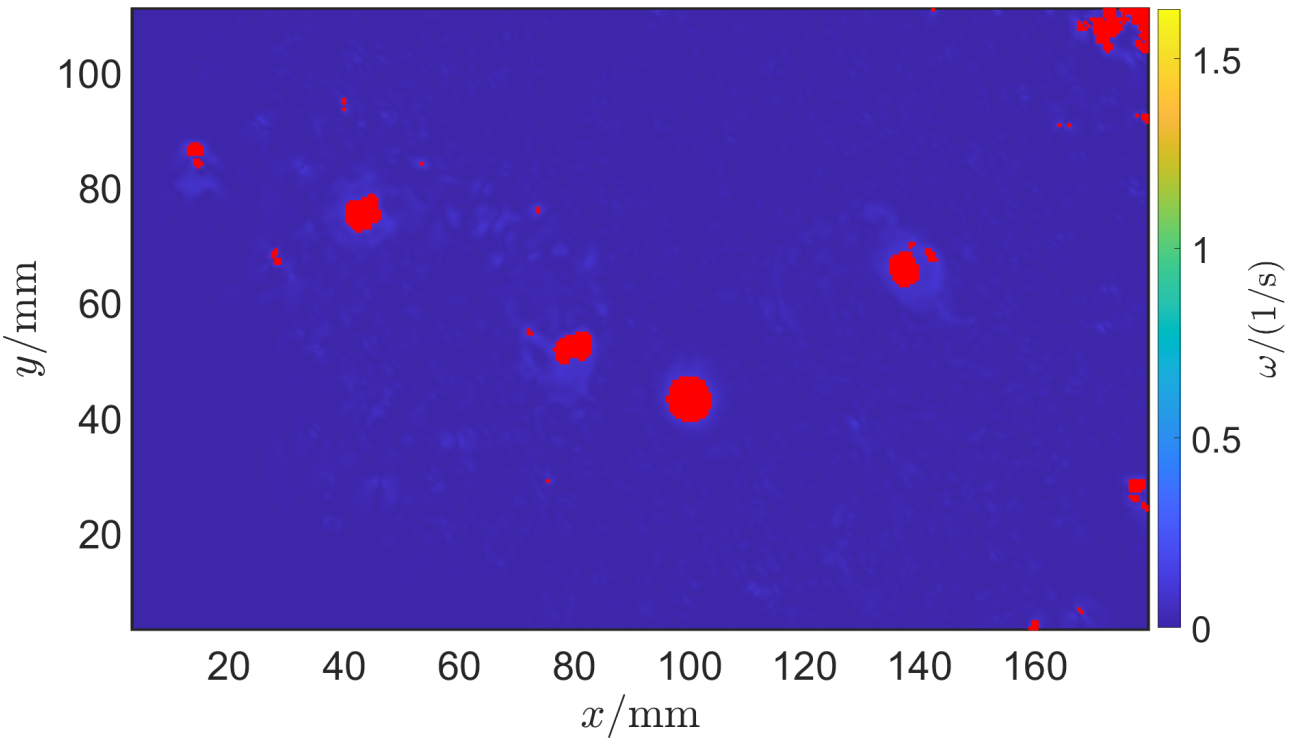

Figure 7.2: ω-criterion ($\omega_{\mathrm{thresh}} = 0.1\ 1/\mathrm{s}$).

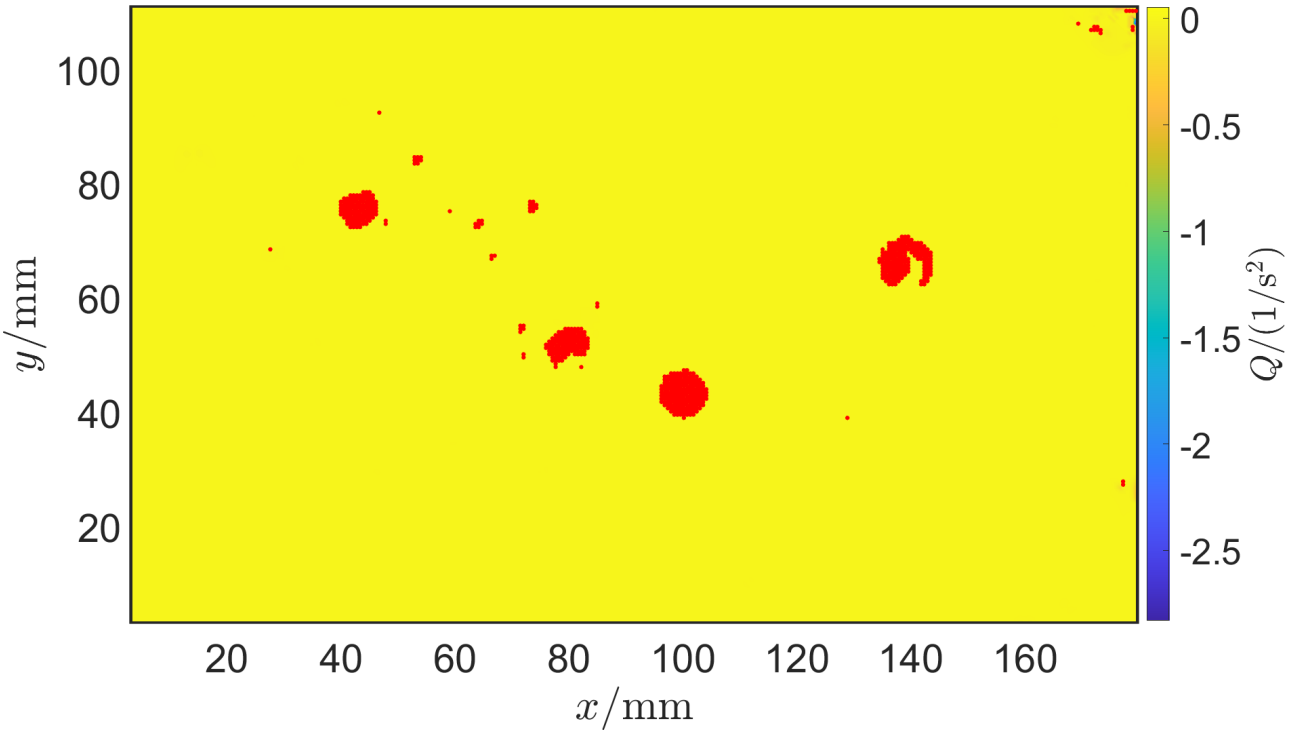

Figure 7.3: Q-criterion ($Q_{\mathrm{thresh}} = 0.001\ 1/\mathrm{s}^2$).

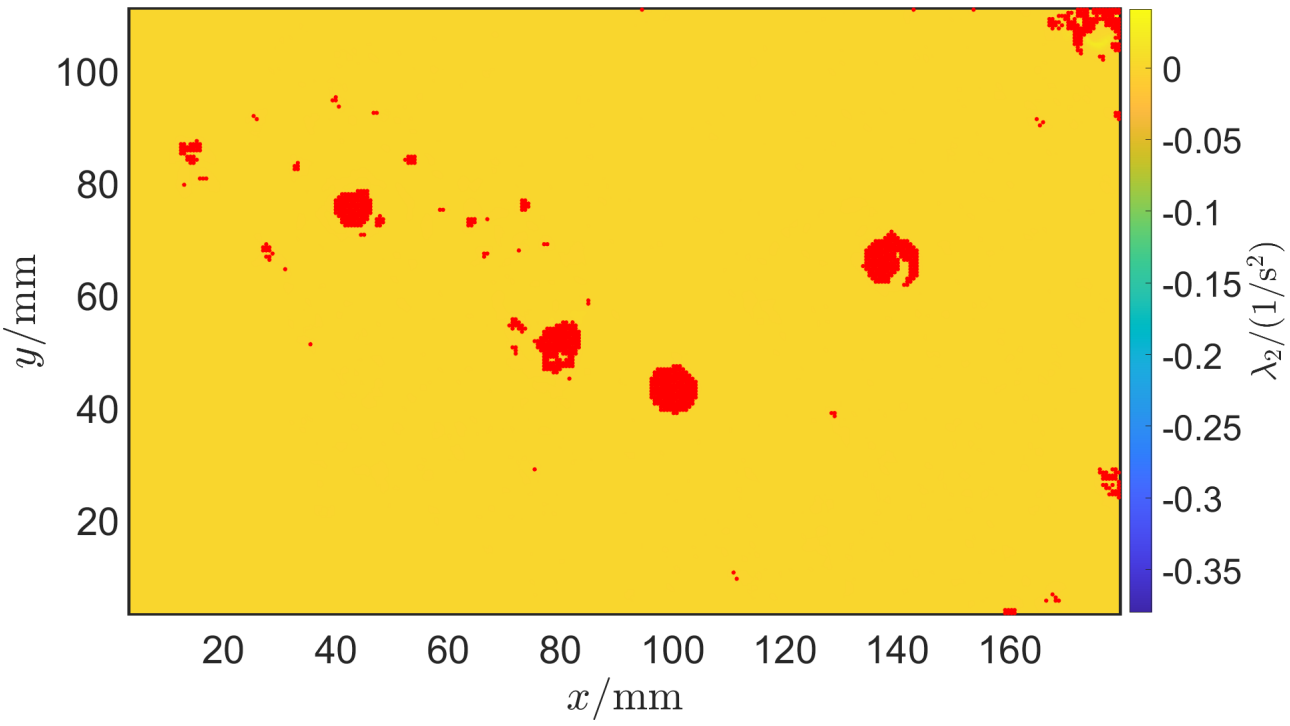

Figure 7.4: λ_2-criterion ($\lambda_{2,\text{thresh}} = -0.001\ 1/\text{s}^2$).

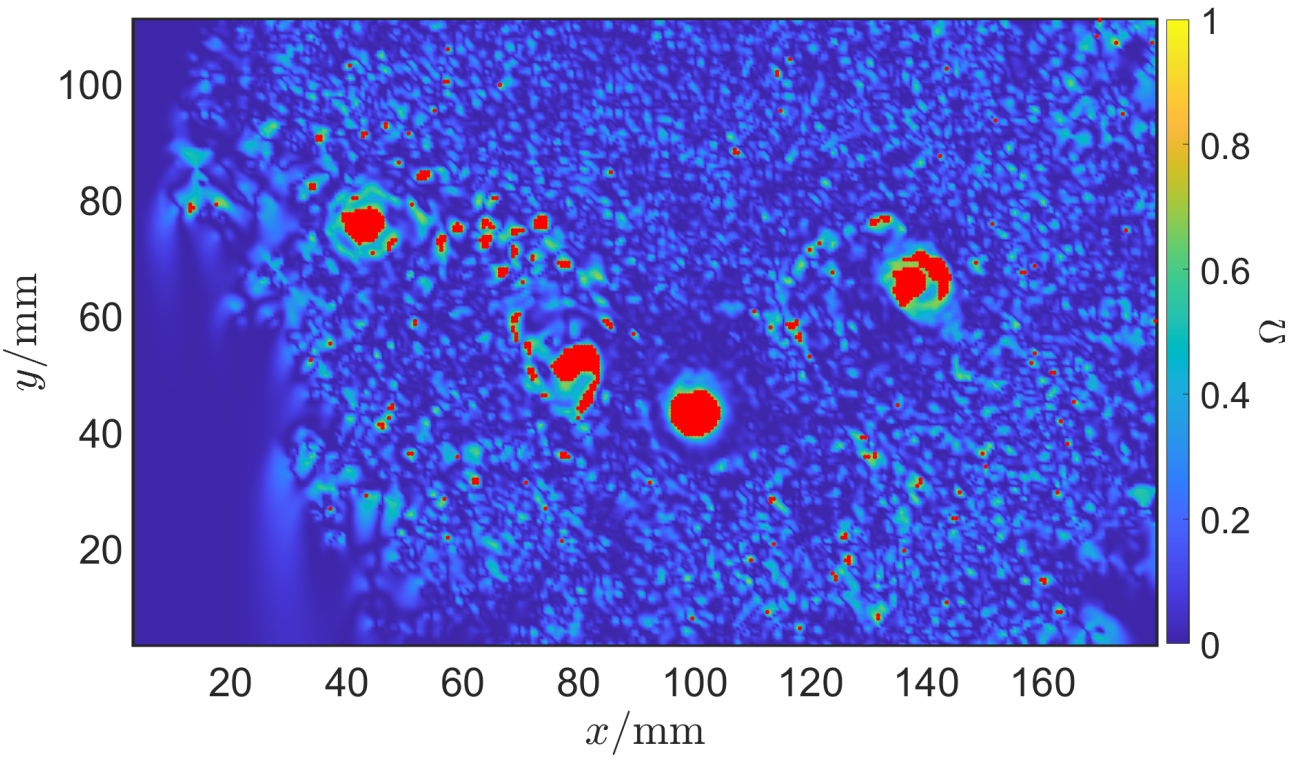

Figure 7.5: Ω-method ($\Omega_{\text{thresh}} = 0.52$).

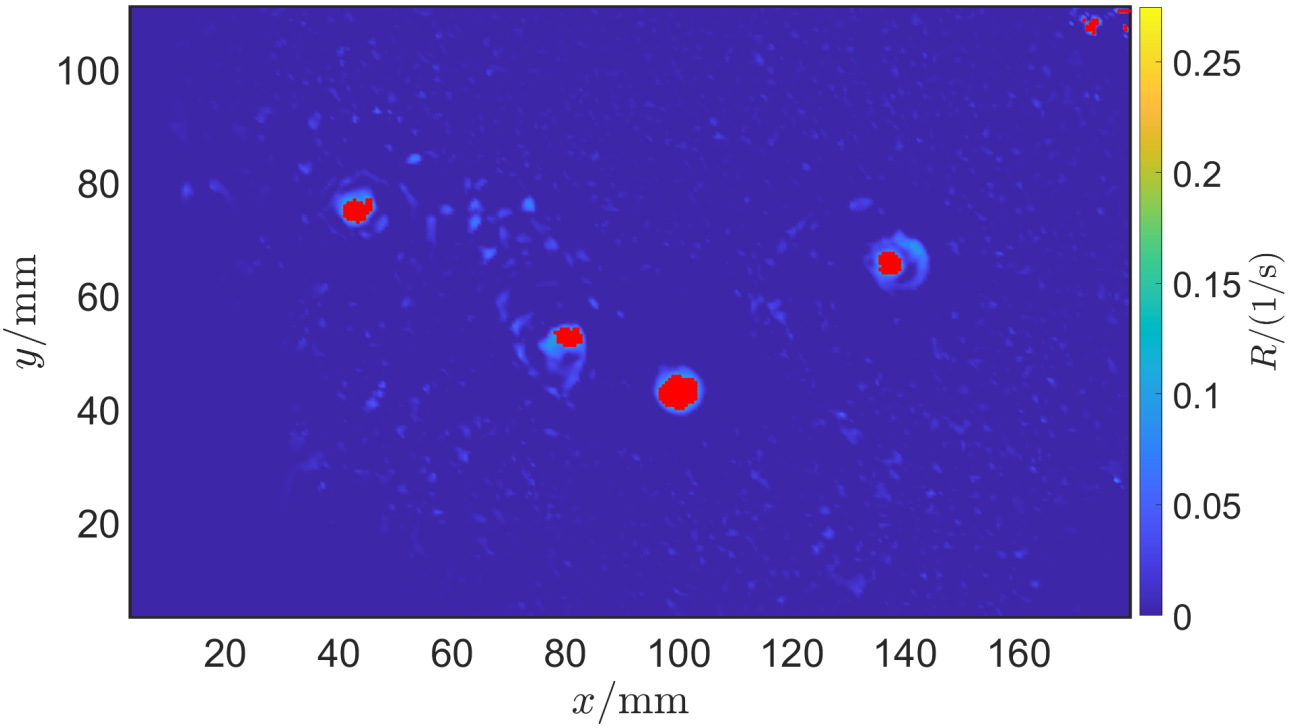

Figure 7.6: Rortex method ($R_{\mathrm{thresh}} = 0.1$ 1/s).

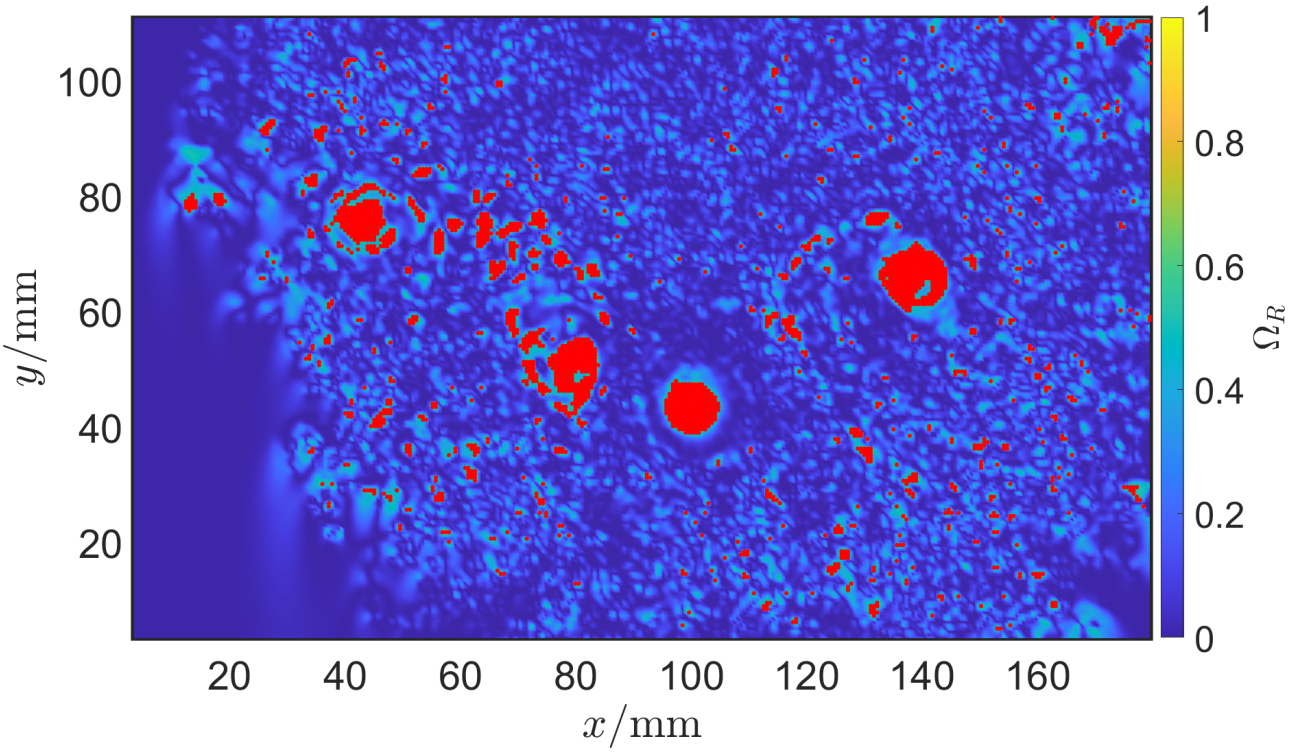

Figure 7.7: Omega-Liutex method ($\Omega_{R,\mathrm{thresh}} = 0.52$).

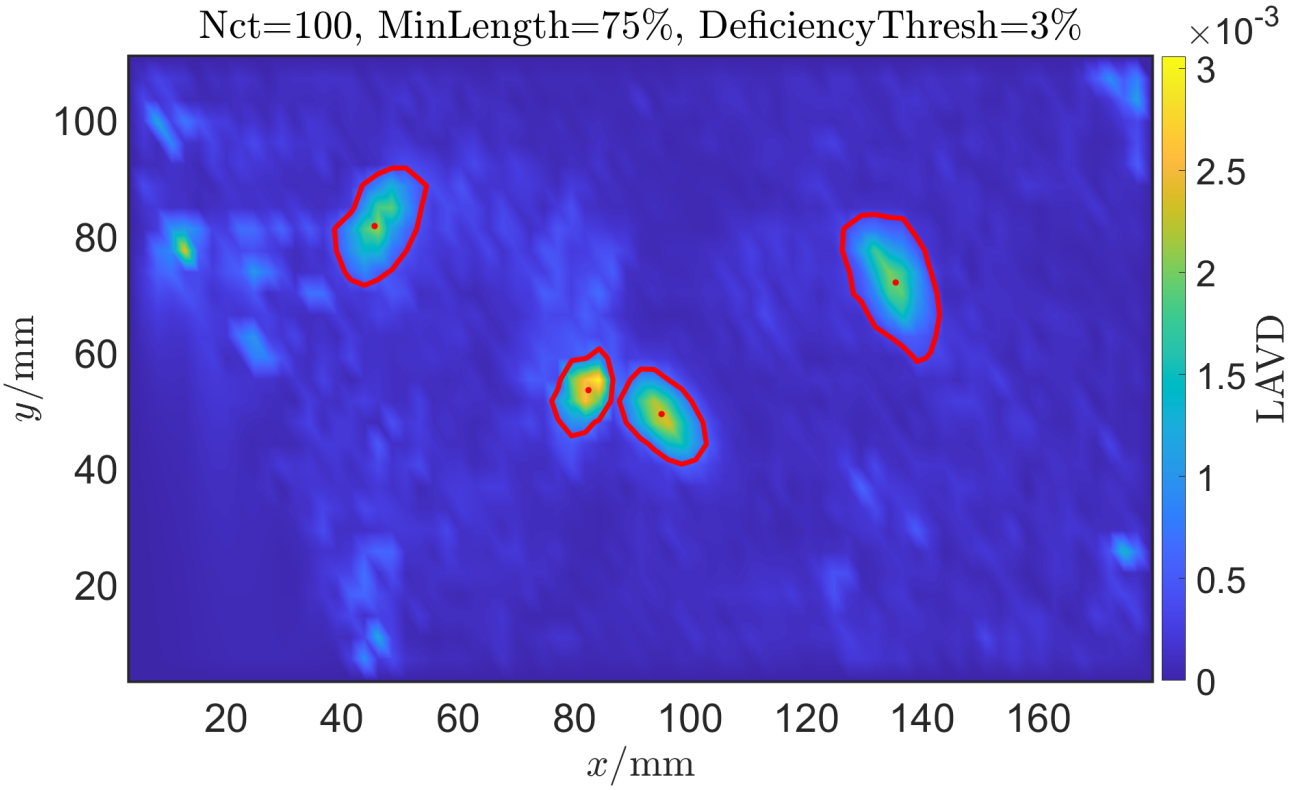

Figure 7.8: LAVD method.

8 Conclusion and future outlook

In the current paper various vortex identification methods were evaluated by applying them to the simulation of three-dimensional fluid flows around cylinder and rectangular cuboid geometries, and also to the simulation of two-dimensional fluid flow around a circular arc cambered plate profile. The methods were also tested on PIV measurement data concerning the generation of vortex rings produced by a vortex cannon. The comparison included both traditional Eulerian local region-type methods – such as the ω-criterion, Q-criterion, and λ_2-criterion – and newer approaches, including the Ω-method, Rortex method, Omega-Liutex method, and the Lagrangian-averaged vorticity deviation (LAVD).

The findings revealed that while traditional methods like the ω-criterion, Q-criterion, and the λ_2-criterion offer simplicity and computational efficiency, they are limited by their reliance on arbitrary threshold values. These thresholds often create challenges in ensuring consistent and accurate vortex detection results. These methods are also prone to shear contamination which could be seen from the detection results as well.

The Ω-method and Omega-Liutex method tried to demonstrate significant improvements by eliminating the need for arbitrary thresholds. However, the empirical 0.52 threshold value is just as arbitrary as the others. Similarly to the ω-criterion, Q-criterion, and the λ_2-criterion, the Ω-method can also be contaminated by shear, and this was reassured by the detection results. Supposedly, both the Rortex method and the Omega-Liutex method should be able to distinguish rotational vortices from shear layers. However, in the examined cases they both encountered issues with shear contamination. In addition, the Rortex method is also dependent on an arbitrary threshold value.

The LAVD method was noted for its robustness to shear contamination, and its ability to identify vortex centers and boundaries. Though the LAVD method did detect some regions with high shear, it was possible to eliminate these regions through the adjustable MinLength parameter. This method's main drawback is its substantial computational demand, requiring significantly more processing time compared to the other methods. As a way to alleviate the computational costs the TRA method (which is also a Lagrangian method) was mentioned. This method is easier to compute and does not require a dense set of initial conditions. The testing of this method is a subject of future research.

In summary, the Ω-method and Omega-Liutex method present practical solutions by addressing threshold-related issues, while the LAVD method offers superior accuracy at the cost of longer computation time. For applications with limited computational resources, methods with simpler implementations such as the Ω-method may be preferred. In contrast, for scenarios where high accuracy is essential, the LAVD method could be advantageous despite its longer processing times.

Future research should focus on refining these methods, potentially exploring hybrid approaches that combine the strengths of different criteria to enhance both accuracy and computational efficiency in vortex detection.

Acknowledgement

I would like to thank my supervisor Dr. Esztella Balla for her constant support and guidance throughout my research. I would also like to express my gratitude to Gábor Daku (Department of Fluid Mechanics) for his help and guidance in connection with the cambered plate simulations. Last but not least, I want to thank Dr. Balázs Istók and Ádám Gyurcsek for providing the PIV measurement data.

The research reported in this paper is part of project no. 143204, implemented with the support provided by the Ministry of Innovation and Technology of Hungary from the National Research, Development and Innovation Fund, financed under the OTKA K 22 funding scheme and project no. TKP-6-6/PALY-2021, implemented with the support provided by the Ministry of Culture and Innovation of Hungary from the National Research, Development and Innovation Fund, financed under the TKP2021-NVA funding scheme.

The work of Kinga Andrea KOVÁCS was supported by the **EKÖP-24-2-BME-193** University Research Scholarship Program of the Ministry for Culture and Innovation from the source of the National Research, Development, and Innovation Fund.

References

[1] Kuldip P Chopra and Lester F Hubert. "Karman vortex streets in wakes of islands." In: *AIAA Journal* 3.10 (1965), pp. 1941–1943.

[2] See Hai Ooi, Azizan Abu Samah, and Peter Braesicke. "A case study of the Borneo Vortex genesis and its interactions with the global circulation". In: *Journal of Geophysical Research: Atmospheres* 116.D21 (2011).

[3] A Andersen et al. "Anatomy of a bathtub vortex". In: *Physical review letters* 91.10 (2003), p. 104502.

[4] Gianni Pedrizzetti et al. "The vortex—an early predictor of cardiovascular outcome?" In: *Nature Reviews Cardiology* 11.9 (2014), pp. 545–553.

[5] Jafar Al-Muhammad et al. "Experimental and numerical characterization of the vortex zones along a labyrinth milli-channel used in drip irrigation". In: *International Journal of Heat and Fluid Flow* 80 (2019), p. 108500.

[6] Yuning Zhang et al. "A review of methods for vortex identification in hydroturbines". In: *Renewable and Sustainable Energy Reviews* 81 (2018), pp. 1269–1285.

[7] Serhiy Yarusevych, Pierre E Sullivan, and John G Kawall. "On vortex shedding from an airfoil in low-Reynolds-number flows". In: *Journal of Fluid Mechanics* 632 (2009), pp. 245–271.

[8] A Chizfahm, E Azadi Yazdi, and M Eghtesad. "Dynamic modeling of vortex induced vibration wind turbines". In: *Renewable Energy* 121 (2018), pp. 632–643.

[9] Esztella Balla, Kinga Andrea Kovács, and Bálint Lendvai. "Comparison of Vortex Detection Methods on the Numerical Simulation of Tip Leakage Flow of a Low-Speed Axial Fan". In: *Turbo Expo: Power for Land, Sea, and Air*. Vol. 87981. American Society of Mechanical Engineers. 2024, V006T10A002.

[10] Mubashshir A Ansari et al. "Vortex micro T-mixer with non-aligned inputs". In: *Chemical Engineering Journal* 181 (2012), pp. 846–850.

[11] Yu-ning Zhang et al. "A selected review of vortex identification methods with applications". In: *Journal of Hydrodynamics* 30 (2018), pp. 767–779.

[12] Qigang Chen et al. "Comparison of vortex identification criteria for planar velocity fields in wall turbulence". In: *Physics of Fluids* 27.8 (2015).

[13] Zihui Zhang et al. "Vortex characteristics of a gas cyclone determined with different vortex identification methods". In: *Powder Technology* 404 (2022), p. 117370.

[14] Wei-wen Zhao, Jian-hua Wang, and De-cheng Wan. "Vortex identification methods in marine hydrodynamics". In: *Journal of Hydrodynamics* 32.2 (2020), pp. 286–295.

[15] Tao Bian et al. "Numerical and experimental investigation of flow loss and flow structure of circular arc cambered plate blade cascade". In: *Proceedings of the Institution of Mechanical Engineers, Part A: Journal of Power and Energy* 233.8 (2019), pp. 961–973.

[16] József Gruber. *Ventilátorok*. Műszaki Kiadó, 1968.

[17] Julian CR Hunt, Alan A Wray, and Parviz Moin. "Eddies, streams, and convergence zones in turbulent flows". In: *Studying turbulence using numerical simulation databases, 2. Proceedings of the 1988 summer program* (1988).

[18] Jinhee Jeong and Fazle Hussain. "On the identification of a vortex". In: *Journal of fluid mechanics* 285 (1995), pp. 69–94.

[19] ChaoQun Liu et al. "New omega vortex identification method". In: *Science China Physics, Mechanics & Astronomy* 59 (2016), pp. 1–9.

[20] Shuling Tian et al. "Definitions of vortex vector and vortex". In: *Journal of Fluid Mechanics* 849 (2018), pp. 312–339.

[21] Xiangrui Dong, Yisheng Gao, and Chaoqun Liu. "New normalized Rortex/vortex identification method". In: *Physics of Fluids* 31.1 (2019).

[22] George Haller et al. "Defining coherent vortices objectively from the vorticity". In: *Journal of Fluid Mechanics* 795 (2016), pp. 136–173.

[23] Brenden Epps. "Review of vortex identification methods". In: *55th AIAA aerospace sciences meeting*. 2017, p. 0989.

[24] David C Banks and Bart A Singer. "Vortex tubes in turbulent flows: identification, representation, reconstruction". In: *Proceedings Visualization'94*. IEEE. 1994, pp. 132–139.

[25] Václav Kolář. "Vortex identification: New requirements and limitations". In: *International journal of heat and fluid flow* 28.4 (2007), pp. 638–652.

[26] Morton E Gurtin. *An introduction to continuum mechanics*. Academic press, 1982.

[27] H Goldstein, CP Poole, and JL Safko. *Classical Mechanics*. Addison Wesley, San Francisco Munich, 2008.

[28] George Haller. "An objective definition of a vortex". In: *Journal of fluid mechanics* 525 (2005), pp. 1–26.

[29] Gianni Astarita. "Objective and generally applicable criteria for flow classification". In: *Journal of Non-Newtonian Fluid Mechanics* 6.1 (1979), pp. 69–76.

[30] Hans J Lugt. "The dilemma of defining a vortex". In: *Recent developments in theoretical and experimental fluid mechanics: Compressible and incompressible flows*. Springer, 1979, pp. 309–321.

[31] Pinaki Chakraborty, Sivaramakrishnan Balachandar, and Ronald J Adrian. "On the relationships between local vortex identification schemes". In: *Journal of fluid mechanics* 535 (2005), pp. 189–214.

[32] Chaoqun Liu et al. "Third generation of vortex identification methods: Omega and Liutex/Rortex based systems". In: *Journal of Hydrodynamics* 31 (2019), pp. 205–223.

[33] Xiang-rui Dong et al. "Determination of epsilon for Omega vortex identification method". In: *Journal of Hydrodynamics* 30 (2018), pp. 541–548.

[34] Yisheng Gao and Chaoqun Liu. "Rortex and comparison with eigenvalue-based vortex identification criteria". In: *Physics of Fluids* 30.8 (2018).

[35] Chaoqun Liu et al. "Rortex—A new vortex vector definition and vorticity tensor and vector decompositions". In: *Physics of Fluids* 30.3 (2018).

[36] Kinga Andrea Kovács and Esztella Balla. "Parameter Identification of the Lagrangian-averaged Vorticity Deviation Vortex Detection Method Through the Investigation of Fluid Flow Around Solid Bodies". In: *Periodica Polytechnica Mechanical Engineering* 67.4 (2023), pp. 293–302.

[37] S Arunachalam and N Lakshmanan. "Across-wind response of tall circular chimneys to vortex shedding". In: *Journal of Wind Engineering and Industrial Aerodynamics* 145 (2015), pp. 187–195.

[38] Peter A Irwin. "Vortices and tall buildings: A recipe for resonance". In: *Physics Today* 63.9 (2010), pp. 68–69.

[39] S Samuel Li and S Kheshtgar Darvazeh. "Suppression of Vortex Shedding from Bridge Pier Using Attached Splitter Plate". In: *Canadian Society of Civil Engineering Annual Conference*. Springer. 2021, pp. 345–356.

[40] Lixia Qu et al. "Quantitative numerical analysis of flow past a circular cylinder at Reynolds number between 50 and 200". In: *Journal of Fluids and Structures* 39 (2013), pp. 347–370.

[41] Dong-Hyeog Yoon, Kyung-Soo Yang, and Choon-Bum Choi. "Flow past a square cylinder with an angle of incidence". In: *Physics of fluids* 22.4 (2010).

[42] Lianfa Wang et al. "Identification of vortex in unstructured mesh with graph neural networks". In: *Computers & Fluids* 268 (2024), p. 106104.

[43] George Haller, Nikolas Aksamit, and Alex P Encinas-Bartos. "Quasi-objective coherent structure diagnostics from single trajectories". In: *Chaos: An Interdisciplinary Journal of Nonlinear Science* 31.4 (2021).

[44] John H McMasters and Michael L Henderson. "Low-speed single-element airfoil synthesis". In: *NASA. Langley Res. Center The Sci. and Technol. of Low Speed and Motorless Flight, Pt. 1* (1979).

[45] Thomas J Mueller and B JANSEN JR. "Aerodynamic measurements at low Reynolds numbers". In: *12th Aerodynamic Testing Conference*. 1982, p. 598.

[46] Moble Benedict et al. "Effect of flow curvature on forward flight performance of a micro-air-vehicle-scale cycloidal-rotor". In: *AIAA journal* 52.6 (2014), pp. 1159–1169.

[47] Justin Winslow et al. "Basic understanding of airfoil characteristics at low Reynolds numbers (10 4–10 5)". In: *Journal of aircraft* 55.3 (2018), pp. 1050–1061.

[48] Witold JF Koning, Wayne Johnson, and Håvard F Grip. "Improved Mars helicopter aerodynamic rotor model for comprehensive analyses". In: *AIAA Journal* 57.9 (2019), pp. 3969–3979.

[49] Richard E Longhouse. "Vortex shedding noise of low tip speed, axial flow fans". In: *Journal of sound and vibration* 53.1 (1977), pp. 25–46.

[50] C Lee, Myung-Kyoon Chung, and Y-H Kim. "A prediction model for the vortex shedding noise from the wake of an airfoil or axial flow fan blades". In: *Journal of sound and vibration* 164.2 (1993), pp. 327–336.

[51] Huashu Dou et al. "An improved prediction model of vortex shedding noise from blades of fans". In: *Journal of Thermal Science* 25.6 (2016), pp. 526–531.

[52] Robert W Paterson et al. "Vortex noise of isolated airfoils". In: *Journal of Aircraft* 10.5 (1973), pp. 296–302.

[53] Thomas F Brooks, D Stuart Pope, and Michael A Marcolini. *Airfoil self-noise and prediction*. Tech. rep. 1989.

[54] Emma C Nash, Martin V Lowson, and Alan McAlpine. "Boundary-layer instability noise on aerofoils". In: *Journal of Fluid Mechanics* 382 (1999), pp. 27–61.

[55] Serhiy Yarusevych and Michael SH Boutilier. "Vortex shedding of an airfoil at low Reynolds numbers". In: *AIAA journal* 49.10 (2011), pp. 2221–2227.

[56] Christopher KW Tam and Hongbin Ju. "Aerofoil tones at moderate Reynolds number". In: *Journal of Fluid Mechanics* 690 (2012), pp. 536–570.

[57] Michele De Gennaro, Helmut Kühnelt, and Alessandro Zanon. "Numerical prediction of the tonal airborne noise for a naca 0012 aerofoil at moderate reynolds number using a transitional urans approach". In: *Archives of Acoustics* 42.4 (2017), pp. 653–675.

[58] EJG Arcondoulis et al. "A review of trailing edge noise generated by airfoils at low to moderate Reynolds number". In: *Acoustics Australia* 38.3 (2010).

[59] Gábor Daku and János Vad. "Experiment-based preliminary design guidelines for consideration of profile vortex shedding from low-speed axial fan blades". In: *Journal of Turbomachinery* 143.6 (2021), p. 061014.

[60] Gábor Daku and János Vad. "A Comprehensive Analytical Model for Vortex Shedding From Low-Speed Axial Fan Blades". In: *Journal of Turbomachinery* 145.7 (2023), p. 071008.

[61] Gábor Daku and János Vad. "Enhanced Modelling of the Phenomenon of Vortex Shedding From a Low-Speed Axial Flow Rotor Blade Profile". In: *Turbo Expo: Power for Land, Sea, and Air*. Vol. 87981. American Society of Mechanical Engineers. 2024, V006T10A005.

Appendix

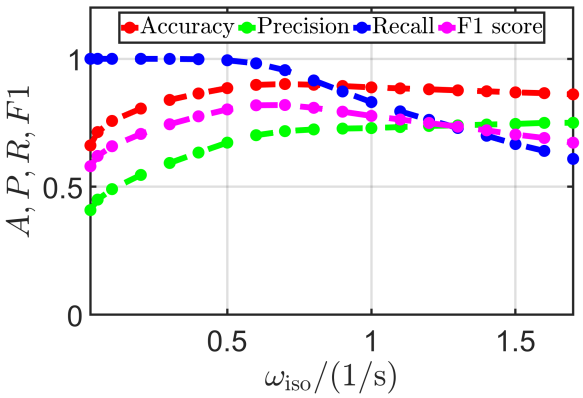

(a) ω-criterion.

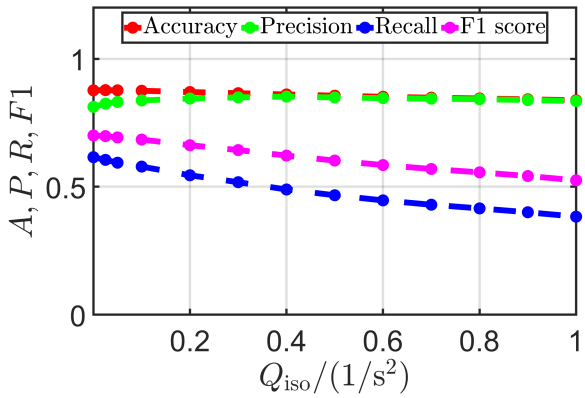

(b) Q-criterion.

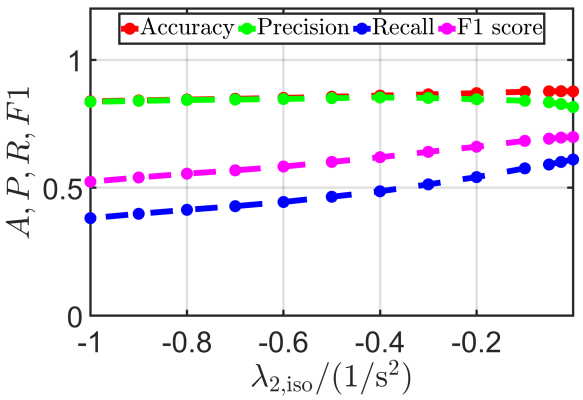

(c) λ_2-criterion.

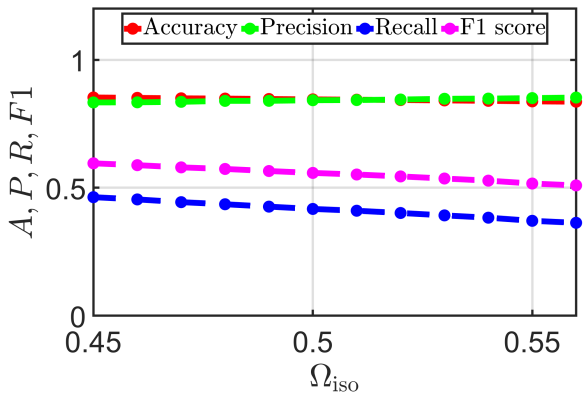

(d) Ω-method.

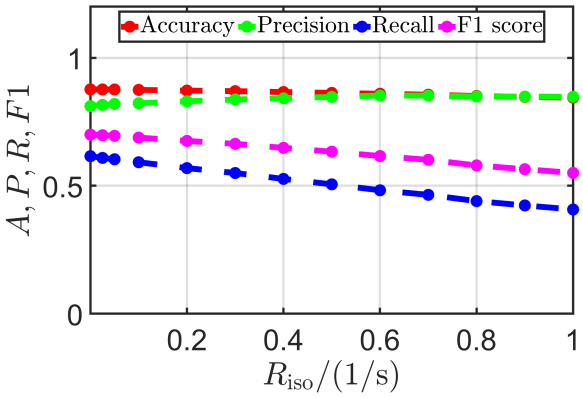

(e) Rortex method.

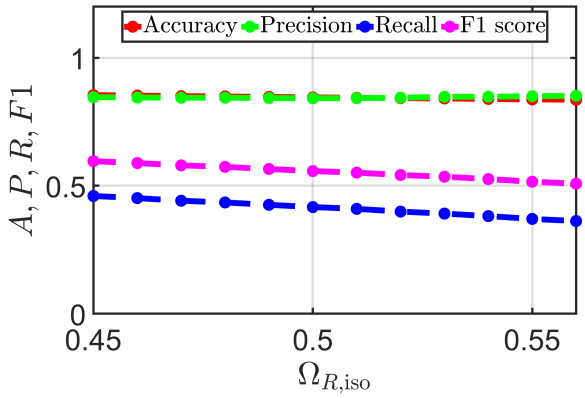

(f) Omega-Liutex method.

Figure 8.1: Metrics as a function of the isovalues (Re = 100, rectangular cuboid, $\theta = 0°$).

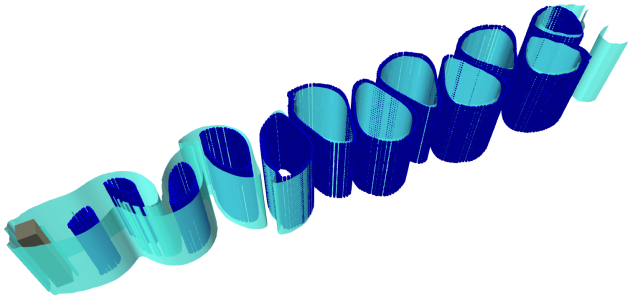

(a) ω-criterion ($\omega_{\text{iso}} = 1.1$ 1/s).

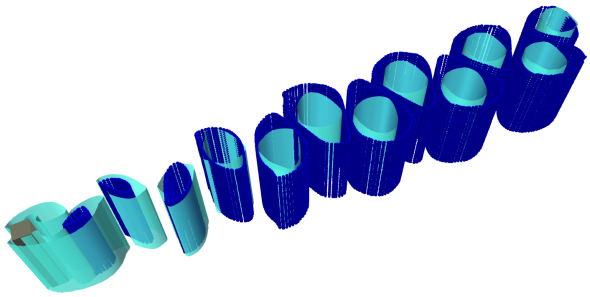

(b) Q-criterion ($Q_{\text{iso}} = 0.5$ 1/s^2).

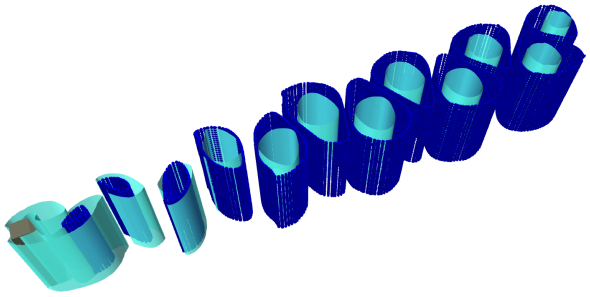

(c) λ_2-criterion ($\lambda_{2,\text{iso}} = -1$ 1/s^2).

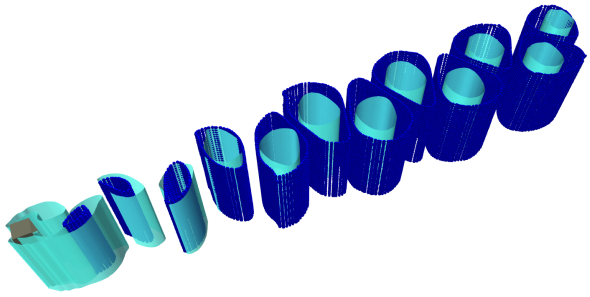

(d) Ω-method ($\Omega_{\text{iso}} = 0.52$).

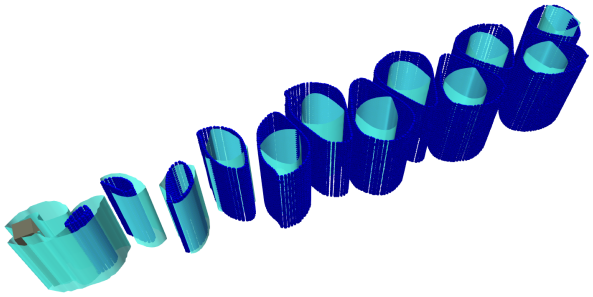

(e) Rortex method ($R_{\text{iso}} = 1$ 1/s).

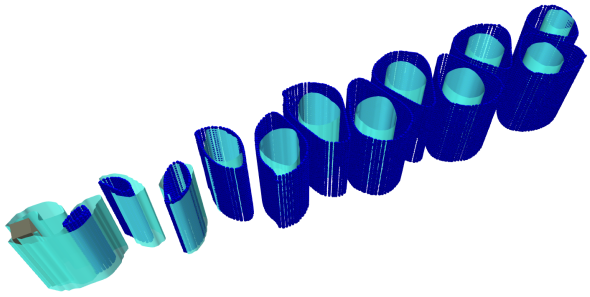

(f) Omega-Liutex method ($\Omega_{R,\text{iso}} = 0.52$).

Figure 8.2: Comparison of vortex detection results (Re = 100, rectangular cuboid, $\theta = 0°$). The LAVD results are denoted by the dark blue dots.

Table 8.1: Sensitivity of the methods to threshold changes (Re = 100, rectangular cuboid, $\theta = 0°$).

	Isovalue 1	Isovalue 2	$\lvert\Delta_{\text{iso}}\rvert$ (%)	$\lvert\Delta_{\text{F1}}\rvert$ (%)
ω-criterion	0.5	1	50	3
Q-criterion	0.5	1	50	15
λ_2-criterion	-0.5	-1	50	15
Ω-method	0.45	0.56	20	17
Rortex method	0.5	1	50	15
Omega-Liutex method	0.45	0.56	20	17

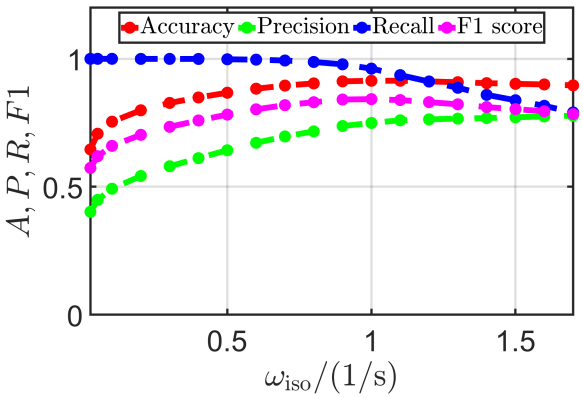

(a) ω-criterion.

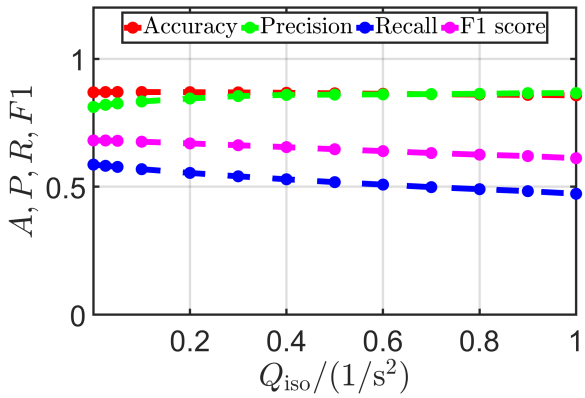

(b) Q-criterion.

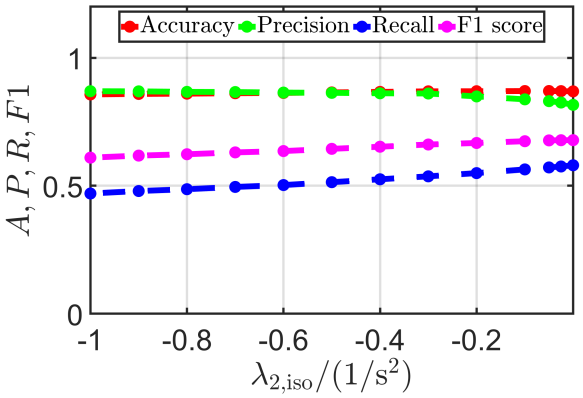

(c) λ_2-criterion.

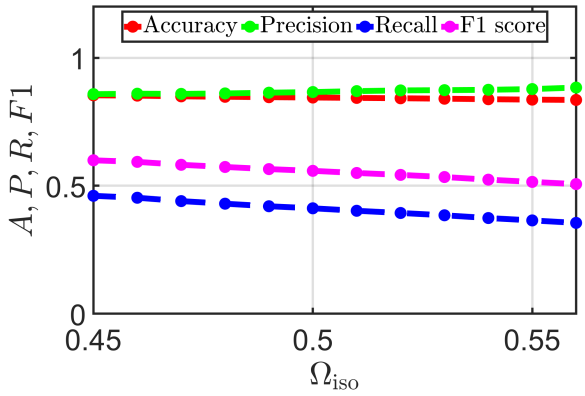

(d) Ω-method.

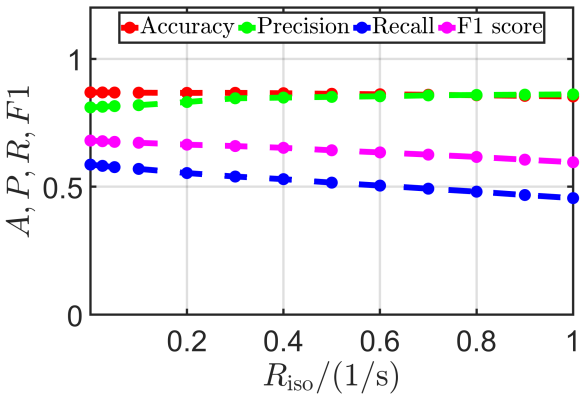

(e) Rortex method.

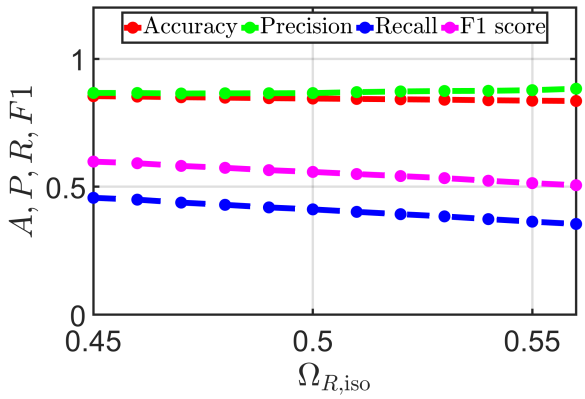

(f) Omega-Liutex method.

Figure 8.3: Metrics as a function of the isovalues (Re = 140, rectangular cuboid, $\theta = 0°$).

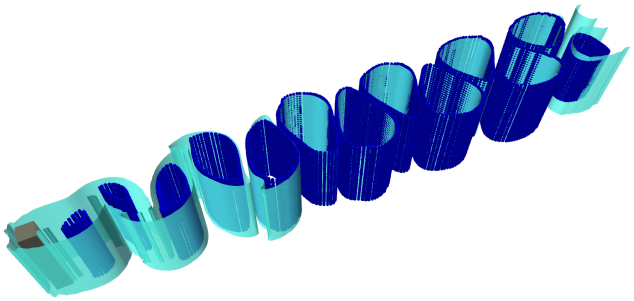

(a) ω-criterion ($\omega_{\text{iso}} = 1.3$ 1/s).

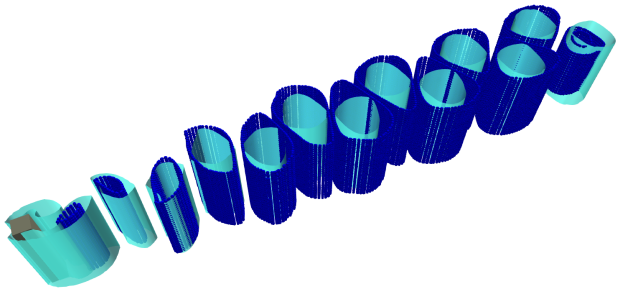

(b) Q-criterion ($Q_{\text{iso}} = 0.5$ 1/s^2).

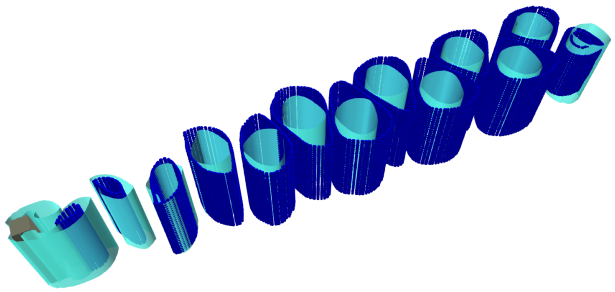

(c) λ_2-criterion ($\lambda_{2,\text{iso}} = -1$ 1/s^2).

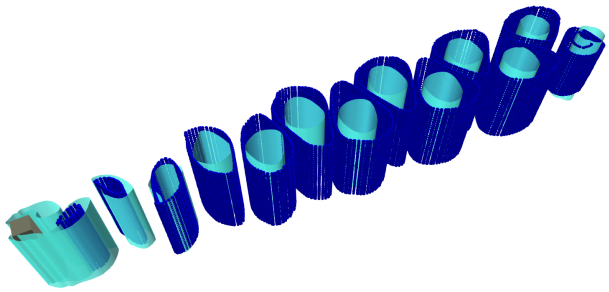

(d) Ω-method ($\Omega_{\text{iso}} = 0.52$).

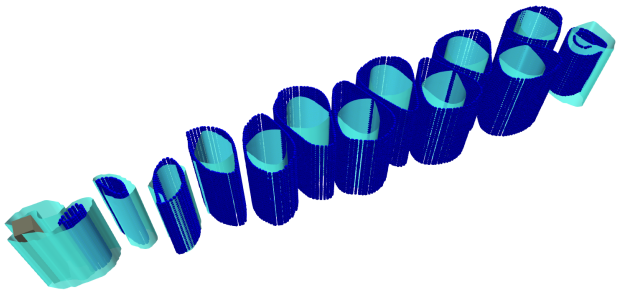

(e) Rortex method ($R_{\text{iso}} = 1$ 1/s).

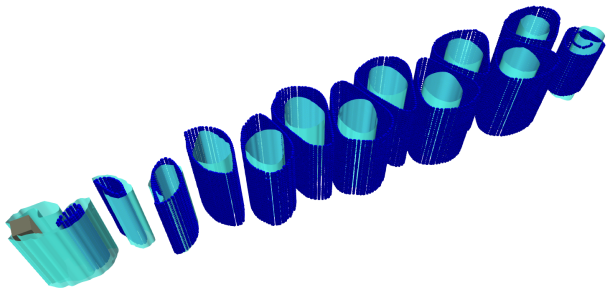

(f) Omega-Liutex method ($\Omega_{R,\text{iso}} = 0.52$).

Figure 8.4: Comparison of vortex detection results (Re = 140, rectangular cuboid, $\theta = 0°$). The LAVD results are denoted by the dark blue dots.

Table 8.2: Sensitivity of the methods to threshold changes (Re = 140, rectangular cuboid, $\theta = 0°$).

	Isovalue 1	Isovalue 2	$\lvert\Delta_{\text{iso}}\rvert$ (%)	$\lvert\Delta_{\text{F1}}\rvert$ (%)
ω-criterion	0.5	1	50	7
Q-criterion	0.5	1	50	6
λ_2-criterion	-0.5	-1	50	6
Ω-method	0.45	0.56	20	18
Rortex method	0.5	1	50	8
Omega-Liutex method	0.45	0.56	20	18

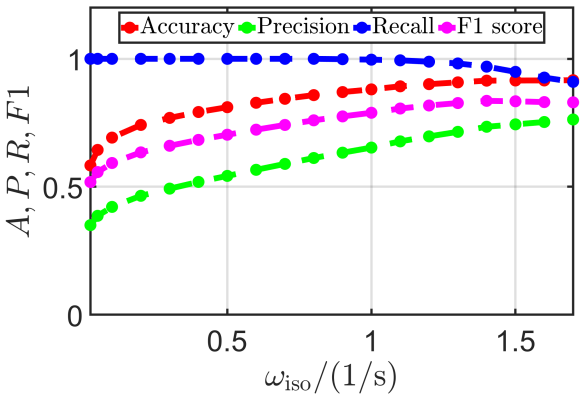

(a) ω-criterion.

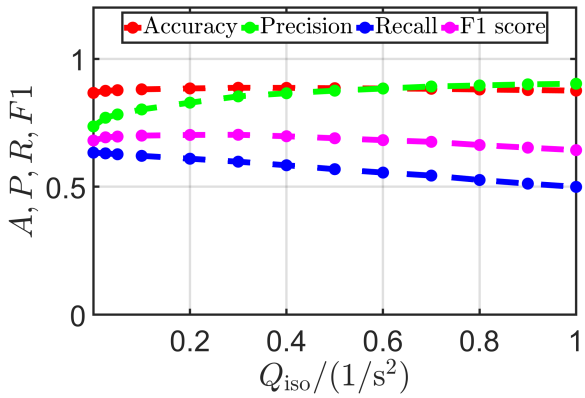

(b) Q-criterion.

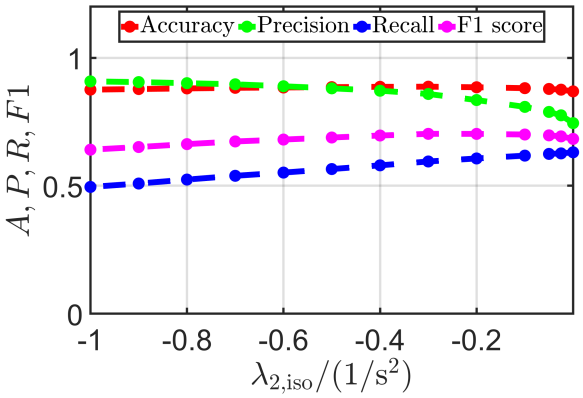

(c) λ_2-criterion.

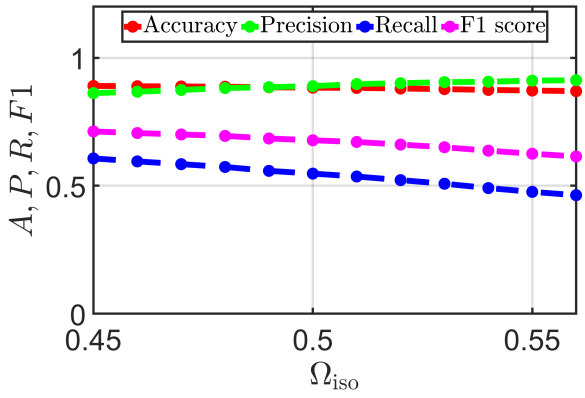

(d) Ω-method.

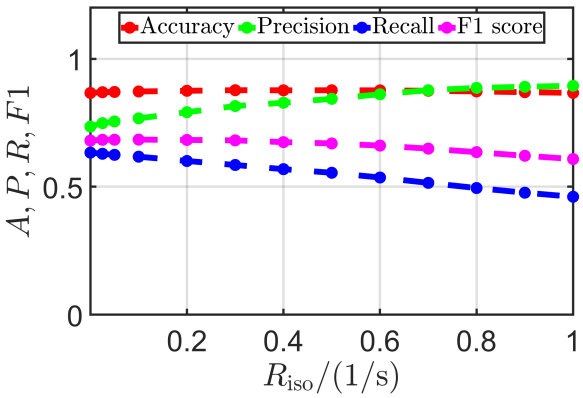

(e) Rortex method.

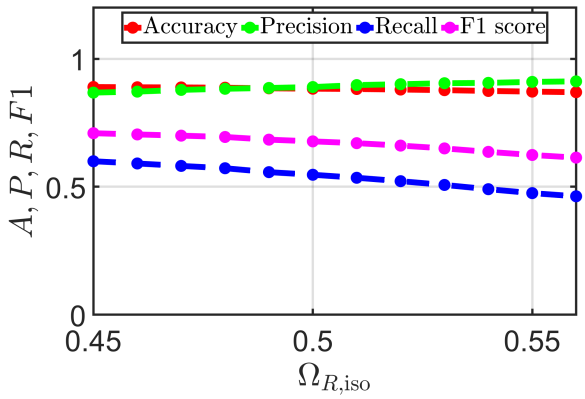

(f) Omega-Liutex method.

Figure 8.5: Metrics as a function of the isovalues (Re = 120, rectangular cuboid, $\theta = 45°$).

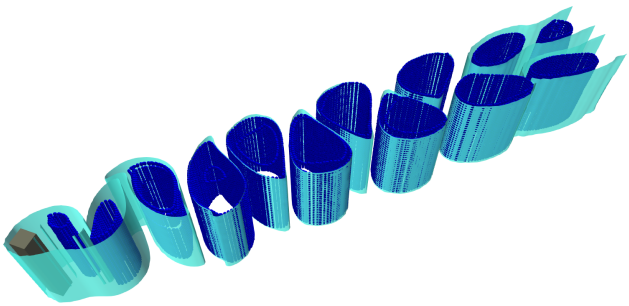

(a) ω-criterion ($\omega_{\text{iso}} = 1.3$ 1/s).

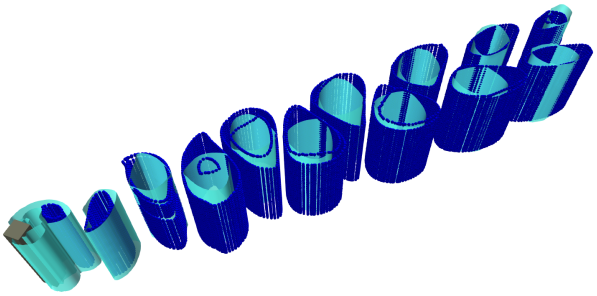

(b) Q-criterion ($Q_{\text{iso}} = 0.6$ 1/s^2).

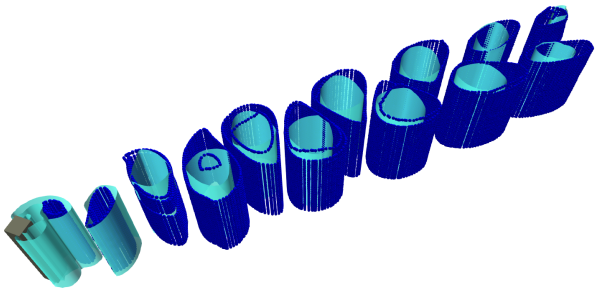

(c) λ_2-criterion ($\lambda_{2,\text{iso}} = -1$ 1/s^2).

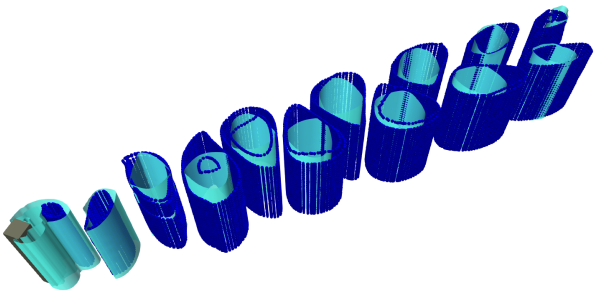

(d) Ω-method ($\Omega_{\text{iso}} = 0.52$).

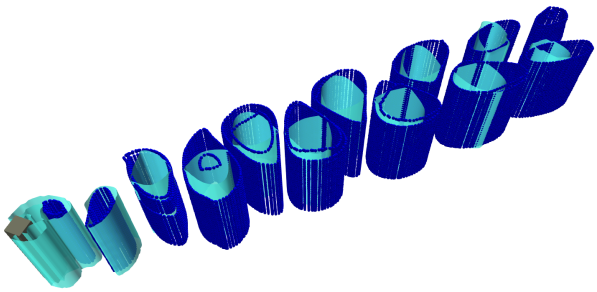

(e) Rortex method ($R_{\text{iso}} = 1$ 1/s).

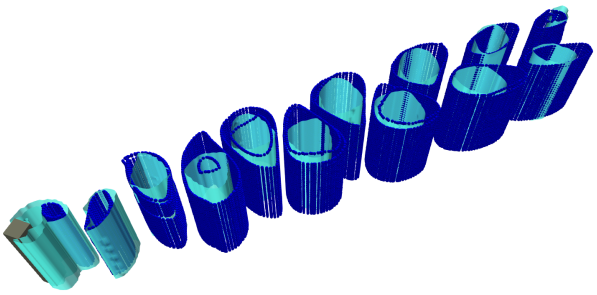

(f) Omega-Liutex method ($\Omega_{R,\text{iso}} = 0.52$).

Figure 8.6: Comparison of vortex detection results (Re = 120, rectangular cuboid, $\theta = 45°$). The LAVD results are denoted by the dark blue dots.

Table 8.3: Sensitivity of the methods to threshold changes (Re = 120, rectangular cuboid, $\theta = 45°$).

	Isovalue 1	Isovalue 2	$\lvert\Delta_{\text{iso}}\rvert$ (%)	$\lvert\Delta_{\text{F1}}\rvert$ (%)
ω-criterion	0.5	1	50	11
Q-criterion	0.5	1	50	7
λ_2-criterion	-0.5	-1	50	7
Ω-method	0.45	0.56	20	16
Rortex method	0.5	1	50	10
Omega-Liutex method	0.45	0.56	20	16